Journal of Materials Chemistry A

ROYAL SOCIETY OF CHEMISTRY

PAPER

View Article Online
View Journal | View Issue

Cite this: *J. Mater. Chem. A*, 2024, **12**, 7693

Reticular design and alkyne bridge engineering in donor–π–acceptor type conjugated microporous polymers for boosting photocatalytic hydrogen evolution†

Mohamed Gamal Mohamed, *[ab] Mohamed Hammad Elsayed,*[cd] Chia-Jung Li,[a] Ahmed E. Hassan,[d] Islam M. A. Mekhemer,[bc] Ahmed Fouad Musa,[c] Mahmoud Kamal Hussien,[eb] Li-Chyong Chen,[efg] Kuei-Hsien Chen,[eh] Ho-Hsiu Chou[c] and Shiao-Wei Kuo *[ai]

Conjugated microporous polymers (CMPs) have gained increased significance as crucial components in the field of photocatalytic H_2 production due to their excellent ultraviolet-visible (UV-vis), and robust fluorescence. Herein, we used two types of reaction approaches including Suzuki and Sonogashira–Hagihara coupling to prepare six different types of CMPs for the first time to investigate and understand the reactivity of triphenylamine (TPA) and alkyne group linked CMPs for photocatalytic H_2 evolution from H_2O. Six different TPA-based CMPs including TPA–TPA (D–D), TPE–TPA (A–D), Py–TPA (A–D), TPA–TB–TPA (D–π–D), TPE–TB–TPA (D–π–A), and Py–TB–TPA (D–π–A) CMPs have been designed and synthesized *via* Suzuki and Sonogashira–Hagihara coupling reaction, respectively. Our investigation of TPA–CMP materials showed that TPA–TPA, Py–TPA, and TPA–TB–TPA CMPs exhibited elevated T_{d10} values, measuring 557 °C, 508 °C, and 482 °C, respectively. Additionally, based on the results of thermal gravimetric analysis (TGA) and nitrogen adsorption–desorption measurements, these CMPs displayed specific surface areas (S_{BET}) of 98, 913, and 459 $m^2\ g^{-1}$, respectively. Furthermore, in the order presented, the Py–TPA, and Py–TB–TPA CMPs showcase hydrogen evolution rate (HER) values of 3633, and 16 700 $\mu mol\ g^{-1}\ h^{-1}$, respectively. As per density functional theory (DFT) calculations, the presence of an alkyne bridge in the Py–TB–TPA CMP can effectively hinder electron–hole recombination, prolong the lifetime of charge carriers, and improve the efficiency of their transfer and separation when compared to a similar CMP (Py–TPA CMP) lacking an alkynyl group. As a result, including an alkynyl (π) bridge in the polymers led to an augmentation in their photocatalytic activity. This work presents various viewpoints regarding the development and architecture of high-performance CMPs incorporating alkynyl groups, showcasing their potential applications in photocatalysis.

Received 27th November 2023
Accepted 19th February 2024

DOI: 10.1039/d3ta07309b

rsc.li/materials-a

Introduction

The extensive reliance on fossil fuels has led to severe energy shortages and environmental challenges, prompting a quest for cleaner, alternative energy solutions.[1–10] To mitigate environmental pollution and tackle our energy crisis, hydrogen (H_2) stands out as an exceptionally eco-friendly and sustainable energy source capable of substantial fossil fuel replacement.[11–16] To address the environmental problems stemming from fossil fuel usage, the most challenging method involves generating

[a]*Department of Materials and Optoelectronic Science, Center for Functional Polymers and Supramolecular Materials, National Sun Yat-Sen University, Kaohsiung 804, Taiwan. E-mail: mgaml.eldin12@yahoo.com; kuosw@faculty.nsysu.edu.tw*

[b]*Department of Chemistry, Faculty of Science, Assiut University, Assiut, Egypt*

[c]*Department of Chemical Engineering, National Tsing Hua University, Hsinchu 30013, Taiwan. E-mail: Mohamed.hammad@azhar.edu.eg*

[d]*Department of Chemistry, Faculty of Science, Al-Azhar University, Nasr City, Cairo 11884, Egypt*

[e]*Center for Condensed Matter Sciences, National Taiwan University, Taipei 10617, Taiwan*

[f]*Center of Atomic Initiative for New Materials, National Taiwan University, Taipei 10617, Taiwan*

[g]*Department of Physics, National Taiwan University, Taipei 10617, Taiwan*

[h]*Institute of Atomic and Molecular Sciences, Academia Sinica, Taipei 10617, Taiwan*

[i]*Department of Medicinal and Applied Chemistry, Kaohsiung Medical University, Kaohsiung 807, Taiwan*

† Electronic supplementary information (ESI) available. See DOI: https://doi.org/10.1039/d3ta07309b

hydrogen through water splitting, with oxygen as the sole byproduct and no CO_2 emissions. Photocatalytic water splitting has garnered significant interest due to its ability to produce high-calorific-value hydrogen, its fuel efficiency, renewability, and lack of pollutants.[17–22] Due to their high activity and appropriate electrical characteristics, a variety of inorganic semiconductors, including selenides, metal oxides, nitrides, and sulfides, have been used as photocatalysts for hydrogen evolution throughout the past several decades.[23–26] Nevertheless, most inorganic photocatalysts face issues like limited absorption bands, challenging synthesis, low activity in visible light, and a scarcity of natural resources.[27–29] Recent research highlights the promising potential of organic semiconductors as a novel class of photocatalysts for H_2 generation, due to their variety of structures, several synthetic pathways, ease of preparation, adaptability, adjustable electronic properties, and tunable band gaps. Consequently, research teams worldwide have shifted their focus toward developing and applying organic photocatalysts, resulting in rapid advancements in this field. Notable examples of these organic polymers include graphitic carbon nitride (g-C_3N_4),[30,31] CMPs,[32–38] covalent triazine frameworks (CTFs),[39–41] polymer dots,[42,43] and metal–organic frameworks (MOFs),[44–46] all of which have been created to produce H_2 from water. Among these options, CMPs have garnered significant attention due to their large easily post-functionalized surface areas, cost-effectiveness, customizable porosities, versatile design, impressive chemical, mechanical, and hydrothermal stabilities, and a wide range of feasible synthetic processes.[47–60] CMPs could be synthesized using various methods such as Schiff base condensation, Suzuki–Miyaura, Sonogashira, Heck coupling processes, mechanochemical synthesis, solvothermal or hydrothermal methods, microwave-assisted synthesis, and more, all of which are both economically viable and user-friendly.[54,57,61–69] Various monomers featuring diverse functional groups, including aldehydes, amines, and halides, can be employed in the synthesis of CMPs. Notably, CMPs exhibit exceptional chemical and physical stability.[54,57] These attributes make CMPs versatile materials suitable for a wide array of applications, including photocatalysis, gas capture and storage, chemical sensing, optoelectronic devices, pollutant adsorption, energy storage, and antibacterial purposes.[54,57] Triphenylamine (TPA)-based materials have found widespread utility due to their inherent redox activity, fluorescence, and the capability to facilitate hole transport *via* radical-cation species. As a result, they are commonly employed as luminescent probes and in the development of molecular electronic materials.[70–72] In comparison to other aromatic materials, TPA exhibits longer π-conjugation, enabling red-shifted emission and absorption spectra.[70] Considerable attention has been directed toward the development of CMPs with D–A or D–π–A architectures. These approaches harness the intrinsic electronic interactions between D and A groups, creating a "push–pull" effect that aids in efficient photoinduced charge separation.[73–75] This mechanism elevates the photocatalytic efficiency of CMPs. In contrast, D–π–A architectures, which rely on enhanced π-electron delocalization, have the potential to further enhance photocatalytic activity by reducing exciton binding energy and promoting exciton dissociation.[76] This is achieved through the utilization of benzene (BZ), benzothiadiazole (BT), dibenzo[*g*,*p*]chrysene (DBC), and pyrene (Py) as the donor, acceptor, and linker components, respectively[76] polymer photocatalysts and photoelectrode materials connected through acetylene linkages have proven to be highly effective in processes such as water splitting and the degradation of contaminants when exposed to visible light irradiation.[77–80] Research carried out by the Chen group has demonstrated that introducing an ethynyl unit into linear conjugated polymers (CPs) leads to improved performance in terms of H_2 generation, photocurrent intensity, and visible light absorption, in contrast to linear CPs lacking an ethynyl unit.[81] Motivated by the findings mentioned above, we proceeded to synthesize a new series of TPA-linked CMPs [namely, TPA–TPA (D–D), TPE–TPA (A–D), Py–TPA (A–D), TPA–TB–TPA (D–π–D), TPE–TB–TPA (D–π–A), and Py–TB–TPA (D–π–A) CMPs], incorporating both acetylene groups and non-acetylene variants, employing a palladium-catalyzed Suzuki and Sonogashira cross-coupling process, as presented in Fig. 1a and 2b. The assessment and analysis of the photocatalytic hydrogen generation performance of these TPA-linked CMPs were carried out with great precision. The T_{d10} values for TPA–TPA, Py–TPA, and TPA–TB–TPA CMPs were notably elevated, with measurements at 557 °C, 508 °C, and 482 °C, respectively through TGA measurements. Moreover, through the use of nitrogen adsorption–desorption investigations, the TPA–TPA, Py–TPA, TPA–TB–TPA and Py–TB–TPA CMPs were found to possess S_{BET} of 98, 913, 459 and 454 $m^2\ g^{-1}$, respectively. In pursuit of the goal of photocatalytic H_2 evolution through water splitting, the entire TPA–CMP series was employed. Among these TPA-linked CMP series, Py–TPA and Py–TB–TPA CMPs displayed impressive hydrogen evolution rates (HER) of 3633 and 16 700 μmol g^{-1} h^{-1}, respectively. Additionally, the Py–TB–TPA CMP exhibited an apparent quantum yield (AQY) of 21.6, 15.8, 14.1, 12.9, and 5.7% at different wavelengths (400, 450, 500, 550, and 600 nm). According to DFT calculations, the Py–TB–TPA CMP emerged as the most efficient CMP photocatalyst, primarily attributed to the advantageous presence of an alkyne bridge. This alkyne bridge effectively suppresses electron–hole recombination, extends the lifespan of charge carriers, and enhances their transfer and separation efficiency.

Experimental

Materials

Triphenylamine (TPA), triethylamine (Et_3N), MeOH, pyrene (Py), trimethylsilyl acetylene (TMS), benzophenone (BZP), Zn powder, $TiCl_4$, acetic acid (AcOH), bromine (Br_2), potassium acetate (KOAc), *N*-bromosuccinimide (NBS), triphenylphosphine (PPh_3), $Pd(PPh_3)_4$, copper(I) iodide (CuI), and magnesium sulfate anhydrous ($MgSO_4$) were purchased from Sigma-Aldrich. Bis(pinacolato)dibron [B_2pin_2], potassium carbonate (K_2CO_3, 99.99%), 1,4-dioxane (DO), *N*,*N*-dimethylformamide (DMF) were ordered from Alfa Aesar. The previously described methods were used to synthesize TPE-4Br, Py-4Br, TPE-T, and Py-T [Scheme S1, S2 and Fig. S1–S6†].[82–87]

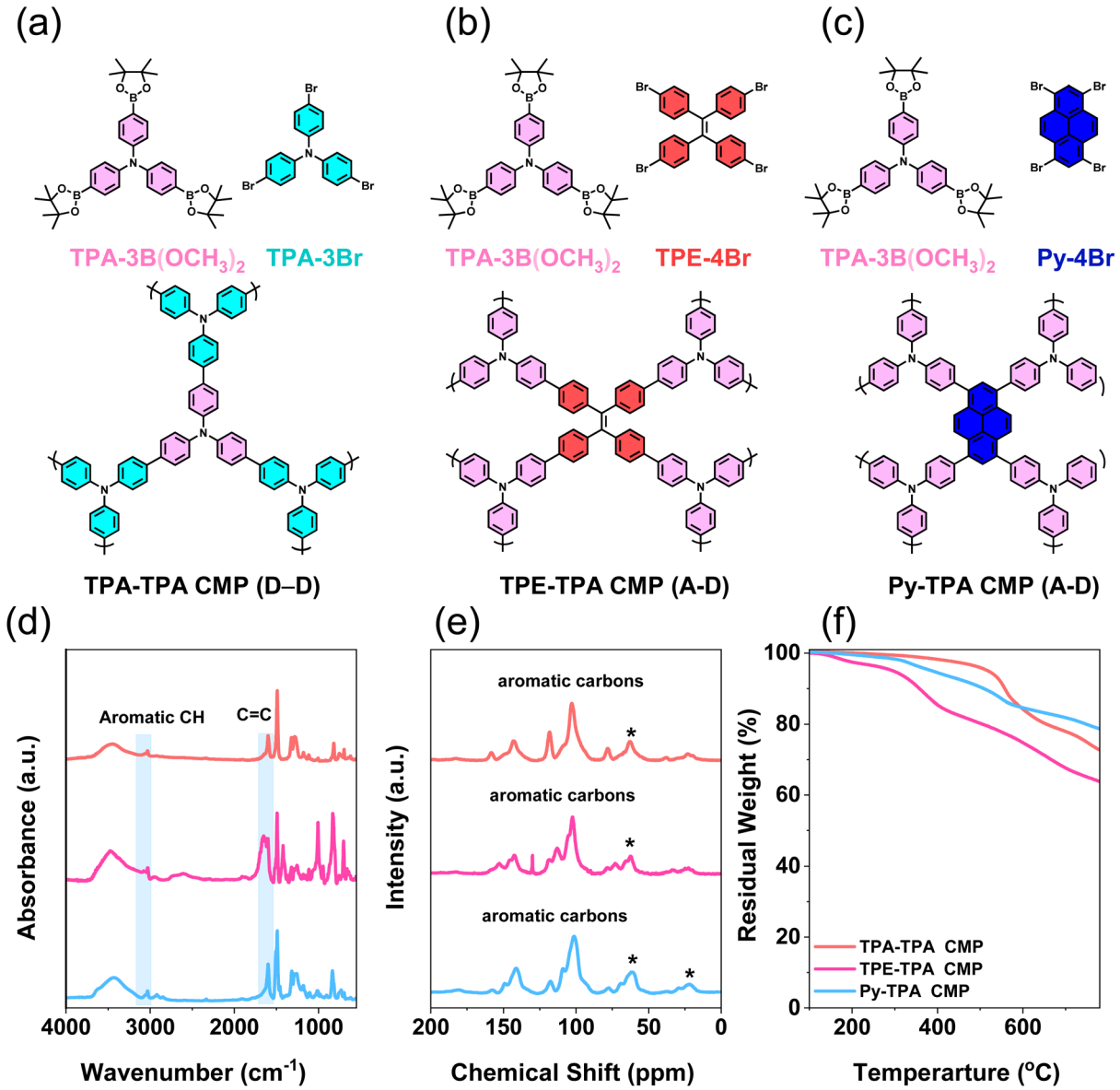

Fig. 1 Synthetic scheme of (a) TPA–TPA, (b) TPE–TPA, and (c) Py–TPA CMPs. (d) FTIR, (e) solid-state NMR, and (f) TGA profiles TPA–TPA, TPE–TPA and Py–TPA CMPs.

Synthesis of tris(4-bromophenyl)amine (TPA-3Br)

Combine 9.56 g of NBS (equivalent to 53.8 mmole) with 50 mL of DMF at 0. Introduce 4 g of TPA (corresponding to 16.32 mmole) into the mixture. After 12 hours of agitation, transfer the mixture into an excess of DI water and let it equilibrate to room temperature. Extract this aqueous solution using $CDCl_3$, followed by rinsing the combined extracts with brine and drying them using anhydrous $MgSO_4$. Gradually decrease the pressure as the solvent evaporates. Utilizing column chromatography on silica gel with *n*-hexane as the eluting solvent to produce TPA-3Br [Scheme S3†] as a white solid, yielding 3.2 g. FTIR (Fig. S7†): 3078, 1618 (C=C). ^{1}H NMR (Fig. S8†): 7.4, 6.92 ppm. ^{13}C NMR (Fig. S9†): 146.7–116.43 ppm.

Synthesis of tris(4-(4,4,5,5-tetramethyl-1,3,2-dioxaborolan-2-yl)phenyl)amine [TPA-3B(OCH$_3$)$_2$]

In a 100 mL round-bottom flask, the following components were introduced: TPA-3Br (4 g, 8.29 mmol), B_2pin_2 (7.77 g, 31.10 mmol), KOAc (14.5 g, 145.10 mmol), $Pd(PPh_3)_4$ (1.04 g), and 100 mL of DO. The mixture was heated to 85 °C and stirred for one day. After completing the reaction, a combination of DCM and DI water was employed to extract the reaction mixture. $MgSO_4$ was added to the mixture, and the organic layer was separated after the drying process. Subsequently, a rotary evaporator was utilized to remove DCM from the mixture. To purify the residue, flash chromatography was carried out using hexane: EA eluent in a 2 : 1 ratio, yielding TPA-3B(OCH$_3$)$_2$ as a creamy yellow solid (2.5 g, Scheme S4†). FTIR (Fig. S10†): 3042, 2981. ^{1}H NMR (Fig. S11†): 7.7, 7.1, 1.40 (36 H). ^{13}C NMR (Fig. S12†): 150.7–22.9 ppm.

Synthesis of tris(4-((trimethylsilyl)ethynyl)phenyl) amine (TPA–TMS)

Dissolving 3 g of TPA-3Br (6.21 mmole) in a solution comprising 40 mL of DCM and 40 mL of Et_3N. To this mixture, add 413.80 mg of $PdCl_2(PPh_3)_2$ and 103.45 mg of CuI. Stir the combination at room temperature for 30 minutes. After this initial stirring period, introduce 6.2 mL of TMS and continue stirring at RT for 30 minutes. Following one day of heating the suspension to 75 °C, allow it to cool to ambient temperature. To purify the TPA–TMS through column chromatography on silica gel with an eluent consisting of *n*-hexane and DCM. This process results in TPA–TMS in a light yellow solid form [Scheme S5†]. FTIR (Fig. S13†): 3043, 2896, 2157 (alkyne unit). ^{1}H NMR (Fig. S14†): 7.33, 6.96, 0.24. ^{13}C NMR (Fig. S15†): 147.41–94.41, 0.3.

Synthesis of tris(4-ethynylphenyl)amine (TPA-T)

Dissolve 3 g of excess K_2CO_3 (equivalent to 21.72 mmole) and 3 g of TPA–TMS (8.43 mmole) in a 30 mL solution with a one-to-one ratio of MeOH and DCM. Stir this mixture at room temperature overnight. The resulting product is then purified, and the solvents from the suspension are removed using column chromatography with a solvent mixture of hexane/EA as the eluent, yielding pure TPA-T as brown powder [Scheme S6†]. FTIR (Fig. S16†): 3266 (C–H alkyne), 3036, 2098 (alkyne unit), 1598. ^{1}H NMR (Fig. S17†): 7.37, 7.02, 3.07. ^{13}C NMR (Fig. S18†): 148.1–117.54, 83.58 (alkyne unit).

Synthesis of TPA–TPA CMP

A gray powder of TPA–TPA CMP [Scheme S7†] was generated by stirring the mixture at 110 °C for three days. This was achieved by adding 150 mg of TPA-3B$(OCH_3)_2$, 129 mg of TPA-3Br, 320 mg of K_2CO_3, and 40 mg of $Pd(PPh_3)_4$ to the same flask containing a solution consisting of 10 mL of DMF and 2 mL of DI water. Subsequently, the flask underwent two rounds of degassing under a vacuum.

Synthesis of TPE–TPA CMP

A light green powder of TPE–TPA [Scheme S8†] was generated by stirring the mixture at 110 °C for three days. This was achieved by adding 128 mg of TPA-3B$(OCH_3)_2$, 100 mg of TPE-4Br, 170 mg of K_2CO_3, and 40 mg of $Pd(PPh_3)_4$ to the same flask containing a solution consisting of 10 mL of DMF and 2 mL of DI water. Subsequently, the flask underwent two rounds of degassing under a vacuum.

Synthesis of Py–TPA CMP

A green powder of Py–TPA [Scheme S9†] was generated by stirring the mixture at 110 °C for three days. This was achieved by adding 240 mg of TPA-3B$(OCH_3)_2$, 150 mg of Py-4Br, 320 mg of K_2CO_3, and 40 mg of $Pd(PPh_3)_4$ to the same flask containing a solution consisting of 10 mL of DMF and 2 mL of DI water. Subsequently, the flask underwent two rounds of degassing under a vacuum. The results of the solubility test indicate that TPA–TPA, TPE–TPA, and Py–TPA CMPs exhibit insolubility in THF, DMF, DCM, and MeOH, as illustrated in Fig. S19a.† This suggests the successful synthesis of these materials is characterized by a high degree of crosslinking density.

Synthesis of TPA–TB–TPA CMP

A coral powder of TPA–TB–TPA CMP [Scheme S10†] was generated by stirring the mixture at 110 °C for three days. This was achieved by adding 66 mg of TPA-T, 100 mg of TPA-3Br, 0.1 g of CuI, 0.1 g of PPh_3, 40 mg of $Pd(PPh_3)_4$ to the same flask containing a solution consisting of 15 mL of DMF and 15 mL of Et_3N. Subsequently, the flask underwent two rounds of degassing under a vacuum.

Synthesis of TPE–TB–TPA CMP

A reddish-brown powder of TPE–TB–TPA CMP [Scheme S11†] was generated by stirring the mixture at 110 °C for three days. This was achieved by adding 56 mg of TPE-T, 100 mg of TPA-3Br, 4.5 mg of CuI, 9.7 mg of PPh_3, 27 mg of $Pd(PPh_3)_4$ to the same flask containing a solution consisting of 15 mL of DMF and 15 mL of Et_3N. Subsequently, the flask underwent two rounds of degassing under a vacuum.

Synthesis of Py–TB–TPA CMP

A dark brown powder of Py–TB–TPA CMP [Scheme S12†] was generated by stirring the mixture at 110 °C for three days. This was achieved by adding 100 mg of Py-T, 216 mg of TPA-3Br, 6.4 mg of CuI, 14 mg of PPh_3, 38 mg of $Pd(PPh_3)_4$ to the same flask containing a solution consisting of 15 mL of DMF and 15 mL of Et_3N. Subsequently, the flask underwent two rounds of degassing under a vacuum. All the CMPs obtained in this study were subjected to a Soxhlet extraction using THF, MeOH, and acetone to eliminate any residual palladium and unreacted monomers from their structures. As depicted in Fig. S19b,† the solubility test outcomes reveal the insolubility of TPA–TB–TPA, TPE–TB–TPA, and Py–TB–TPA CMPs in THF, DMF, DCM, and MeOH. This suggests that the successful production of these materials is marked by a notable high crosslinking density.

Results and discussion

Synthesis and characterization of TPA-linked CMPs

In this research, a high-yield synthesis yielded a creamy yellow solid by combining TPA-3Br with B_2pin_2, KOAc, and DO in the presence of $Pd(PPh_3)_4$. This reaction resulted in the formation of the building block monomer TPA-3B$(OCH_3)_2$ [Scheme S4†]. The TPA-T monomer was prepared in a two-step process: initially, a yellow powder named TPA–TMS [Scheme S6†] was generated by reacting TPA-3Br with TMS and CuI in the presence of THF, Et_3N, and $Pd(PPh_3)_4$. Subsequently, the hydrolysis of TPA–TMS was carried out using a mixture of MeOH and DCM solvents in the presence of K_2CO_3 to produce TPA-T [Scheme S6†]. Six different TPA-linked CMP materials (CMPs) were synthesized for photocatalytic H_2 evolution from H_2O. Firstly, TPA–TPA (D–D), TPE–TPA (A–D), and Py–TPA (D–A) CMPs were prepared using the Suzuki coupling reaction. In

this method, brominated TPA, TPE, and Py were coupled with TPA-3B$(OCH_3)_2$ in the presence of a catalyst and K_2CO_3, as illustrated in Fig. 1a–c. All CMP samples were washed with methanol using Soxhlet extraction to remove the traces of $Pd(PPh_3)_4$. Fig. S20–S22† and 1d illustrate the FTIR spectra of the TPA-3B$(OCH_3)_2$, TPA-3Br, TPE-4Br, Py-4Br, TPA–TPA CMP, TPE–TPA CMP, and Py–TPA CMP. When analyzed at ambient temperature, the FTIR spectra revealed common characteristics across all TPA-3B$(OCH_3)_2$, TPA-3Br, TPE-4Br, Py-4Br and TPA-linked CMPs. Specifically, TPA–TPA, TPE–TPA, and Py–TPA CMPs exhibited absorption signals in the vicinity of 3303 cm^{-1}, which can be attributed to the presence of water absorbed within their framework, leading to OH stretching vibrations. Distinctive peaks at approximately 3057–3024 cm^{-1} were observed, representing the C–H aromatic stretching vibrations for TPA-3B$(OCH_3)_2$, TPA-3Br, TPE-4Br, Py-4Br, TPA–TPA CMP, TPE–TPA CMP, and Py–TPA CMP. while a peak at around in the range 1606–1621 cm^{-1} indicated the C=C stretching vibrations within these materials. The structural verification of the TPA–TPA, TPE–TPA, and Py–TPA CMPs was carried out using solid-state ^{13}C NMR spectroscopy, and the results are illustrated in Fig. 1e. Across all TPA–TPA, TPE–TPA, and Py–TPA CMPs materials, carbon signals in the range of 142.61–103.16 ppm were observed, and these signals corresponded to the aromatic carbons within the materials.

Thermogravimetric analysis (TGA) was utilized to explore the thermal stability of the synthesized TPA-3B$(OCH_3)_2$, TPA-3Br, TPE-4Br, Py-4Br, TPA–TPA CMP, TPE–TPA CMP, and Py–TPA CMP at an elevated temperature of 800 °C, as depicted in Fig. 1f, S23 and Table S1.† The T_{d5} and T_{d10} values for TPA–TPA CMP were determined to be 518 °C and 558 °C, respectively, resulting in a char yield of 73 wt%. Similarly, TPE–TPA CMP exhibited thermal degradation temperatures with T_{d5} and T_{d10} values of 296 °C and 358 °C, along with a char yield of 64%. Py–TPA CMP showed T_{d5} and T_{d10} values of 387 °C and 508 °C, respectively, with a char yield of 79 wt%. Fig. S23† demonstrates that the

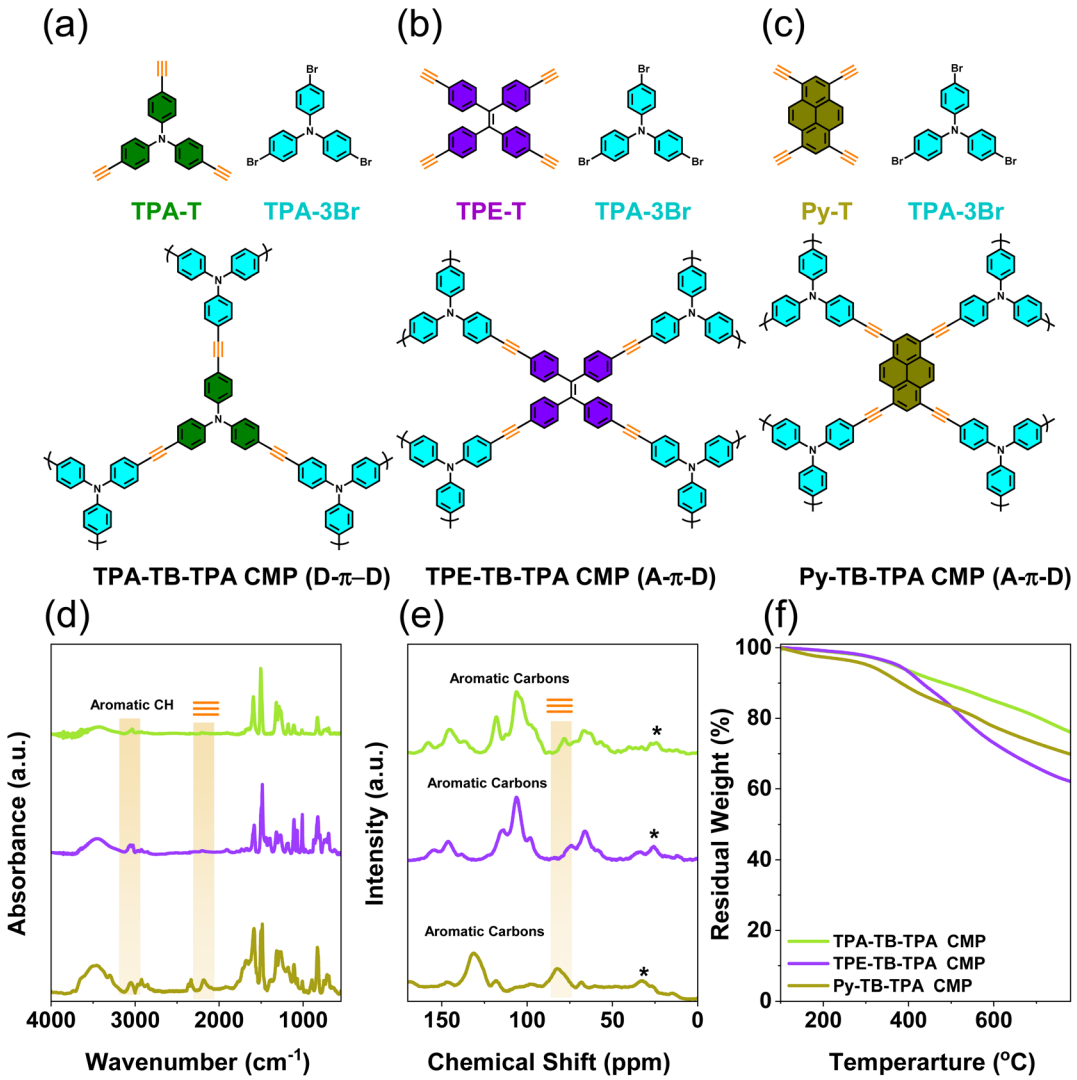

Fig. 2 Synthetic scheme of (a) TPA–TB–TPA, (b) TPE–TB–TPA and (c) Py–TB–TPA CMPs. (d) FTIR, (e) solid-state NMR, and (f) TGA profiles TPA–TB–TPA, TPE–TB–TPA, and Py–TB–TPA CMPs.

synthesized TPA–TPA CMP, TPE–TPA CMP, and Py–TPA CMP displayed enhanced thermal stability when compared to their monomers. For the preparation of TPA–TB–TPA CMP, TPE–TB–TPA CMP, and Py–TB–TPA CMP with acetylene group as π linker (Fig. 2a–c), the synthesis involved the Sonogashira coupling reaction. In this case, brominated TPA was coupled with ethynyl TPA, TPE, and Py in a mixture of DMF/Et_3N in the presence of Pd as a catalyst. The FTIR spectra in Fig. S24–S26† and 2d depict the characteristics peaks of TPA-T, TPA-3Br, TPE-T, Py-T, TPA–TB–TPA CMP, TPE–TB–TPA CMP, and Py–TB–TPA CMP. The absorption bands corresponding to alkyne CH and alkyne triple bond were observed within the range of 3279–3266 cm^{-1} and 2186–2098 cm^{-1}, respectively, for all TPA-T, TPE-T, and Py-T compounds. A room temperature FTIR analysis revealed that all three CMPs, TPA–TB–TPA, TPE–TB–TPA, and Py–TB–TPA, exhibited similar spectral features. Notably, they exhibited absorption peaks at approximately 3472 cm^{-1}, attributed to OH stretching vibrations resulting from water absorbed in their structure. Furthermore, distinctive peaks were observed in the range of 3086 to 3042 cm^{-1}, corresponding to aromatic stretching vibrations of C–H bonds.

In the FTIR spectra of TPA–TB–TPA CMP, TPE–TB–TPA CMP, and Py–TB–TPA CMP, moderate absorption signals were observed with a center at 2193 cm^{-1}. This absorption pattern was attributed to the presence of internal and terminal alkyne groups in the structure of these samples, as illustrated in Fig. 2d. In summary, the FTIR spectra provided valuable insights into the structural and chemical properties of these CMPs, revealing the presence of water, aromatic C–H stretching vibrations, C=C stretching vibrations, and the influence of alkyne groups on the spectra of the specific CMPs. Solid-state ^{13}C NMR spectroscopy was employed to confirm the structural composition of the TPA–TB–TPA CMP, TPE–TB–TPA CMP, and Py–TB–TPA CMP samples, and the results are presented in Fig. 2e. In all CMP materials, carbon signals were detected in the range of 142.61–103.16 ppm, corresponding to the aromatic carbons within these materials. Notably, in the NMR spectra of TPA–TB–TPA CMP, TPE–TB–TPA CMP, and Py–TB–TPA CMP, a distinctive resonance peak was observed at approximately 80.26 ppm. This peak is a clear indication of the presence of alkyne groups incorporated into the framework of these specific CMPs. In summary, the NMR and FTIR analyses collectively provide robust evidence confirming the successful synthesis of the six TPA–CMPs.

The thermal stability based on TGA [Fig. 2f and Table S1†] revealed that the T_{d5} and T_{d10} of TPA–TB–TPA CMP, were found to be 370 °C and 483 °C, respectively, and the char yield was 76 wt%. TPE–TB–TPA–CMP displayed T_{d5} and T_{d10} values of 376 °C and 432 °C, with a char yield of 63 wt%. Finally, Py–TB–TPA CMP demonstrated T_{d5} and T_{d10} values of 306 °C and 382 °C, along with a char yield of 70 wt%. Additionally, Fig. S27† illustrates that TPA–TB–TPA, TPE–TB–TPA, and Py–TB–TPA CMPs exhibit higher thermal decomposition temperatures (T_d) in comparison to their respective monomers [TPA-T, TPA-Br_3, TPE-T, and Py-T]. The Suzuki and Sonogashira coupling method yielded six unique CMPs, each characterized by its distinct chemical structure and tailored properties, making them well-suited for the photocatalytic generation of H_2 from water. The overall XPS survey spectra for TPA-3B$(OCH_3)_2$, TPA-3Br, TPA-T, TPA–TPA CMP, TPE–TPA CMP, Py–TPA CMP, TPA–TB–TPA CMP, TPE–TB–TPA CMP, and Py–TB–TPA CMP reveal the presence of nitrogen (N), and carbon (C) atoms, as confirmed in Fig. S28 and S29.† C atoms can be observed in the comprehensive XPS survey spectra of TPE-4Br, Py-4Br, TPE-T, and Py-T, as illustrated in Fig. S28 and S29.† Fig. S30† illustrates that the synthesized TPA-3B$(OCH_3)_2$, TPA-T, TPA-3Br, TPE-4Br, and Py-4Br exhibit crystalline characteristics. As evidenced by the XRD data [Fig. S31†], The absence of crystalline peaks and long-range organization, along with the presence of an amorphous aggregation structure, characterizes all the synthesized TPA-linked CMPs. This could be attributed to the uncontrolled expansion of the framework resulting from irreversible kinetic control during the TPA–CMP polymerization process. The XRD data has confirmed the synthesis of TPA–CMPs. The BET-specific surface areas (S_{BET}), pore diameters, and total pore volumes (V_{total}) of TPA–TPA, TPA–TPE, TPA–Py, TPA–TB–TPA, TPE–TB–TPA, and Py–TB–TPA CMPs were determined through N_2 measurements at a temperature of 77 K, as depicted in Fig. 3a–f. The BET tests yielded type I isotherms, indicating the presence of mesoporous structures in these CMPs. Additionally, microporous behavior was observed, characterized by a significant increase occurring at very low-pressure levels (P/P_0 = 0–0.1). Moreover, S_{BET} and V_{total} for each CMP were as follows: TPA–TPA–CMP had S_{BET} and V_{total} values of 98 $m^2\ g^{-1}$ and 0.22 $cm^3\ g^{-1}$, TPA–TPE CMP exhibited values of 423.4 $m^2\ g^{-1}$ and 0.69 $cm^3\ g^{-1}$, TPA–Py CMP showed S_{BET} and V_{total} values of 913 $m^2\ g^{-1}$ and 0.62 $cm^3\ g^{-1}$, TPA–TB–TPA CMP had corresponding values of 459 $m^2\ g^{-1}$ and 0.25 $cm^3\ g^{-1}$, TPE–TB–TPA–CMP had values of 487 $m^2\ g^{-1}$ and 0.57 $cm^3\ g^{-1}$, and Py–TB–TPA CMP demonstrated S_{BET} and V_{total} values of 454 $m^2\ g^{-1}$ and 0.28 $cm^3\ g^{-1}$, respectively. Nonlocal density functional theory (NL-DFT) was employed to assess the pore sizes of the CMPs. The pore size distribution curves revealed that TPA–TPA CMP, TPE–TPA CMP, Py–TPA CMP, TPA–TB–TPA CMP, TPE–TB–TPA CMP, and Py–TB–TPA CMP materials had pore diameters of 0.4, 1.0, 1.0, 1.0, 1.1, and 1.1 nm, respectively. SEM and HR-TEM were employed to analyze the structure, organization, and porosity characteristics of TPA–CMPs, as depicted in Fig. 4a–l. SEM examinations revealed the formation of irregularly aggregated nanospheres in TPA–TPA CMP, TPE–TPA CMP, TPA–TB–TPA CMP, and TPE–TB–TPA CMP and Py–TB–TPA CMP, as presented in Fig. 4a, b and d–f. In contrast, Py–TPA CMP exhibited well-defined rod-like structures with a hairy architecture [Fig. 4c and S32†]. The HR-TEM images of the as-prepared TPA–CMPs and TPA–TB–CMPs, as illustrated in Fig. 4g–l, displayed a lack of long-range ordering and consistently sized pores. The presence of dark dots in the TEM images is attributed to small traces of the Pd catalyst within the framework of the CMPs. The confirmation of the presence of C, N, and Pd elements in all CMP materials was established through SEM-EDS mapping, as depicted in Fig. S33 and S34.†

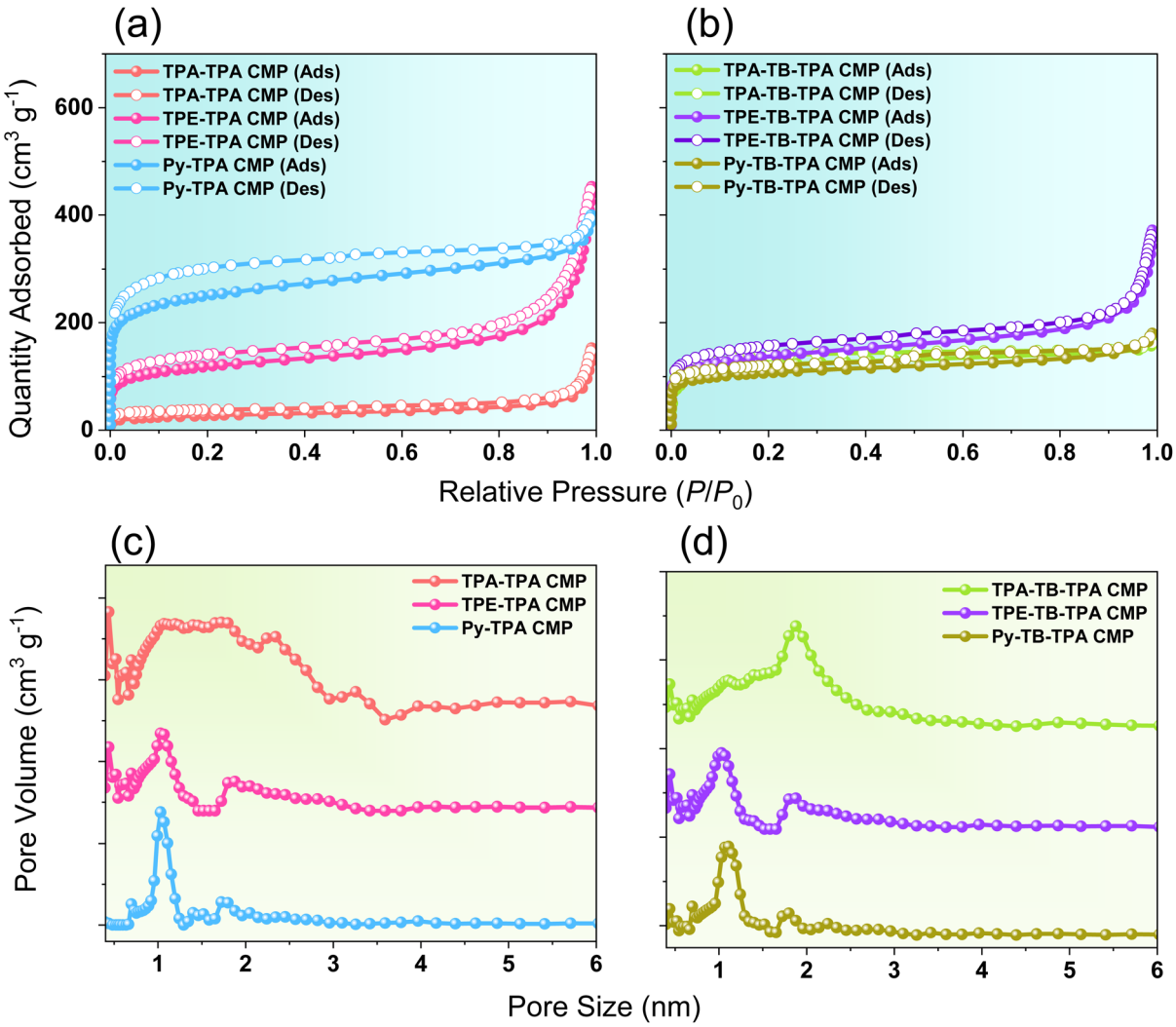

Fig. 3 (a and c) N_2 sorption isotherms and (b and d) pore size profiles are provided for the following CMPs: TPA–TPA, TPE–TPA, Py–TPA, TPA–TB–TPA, TPE–TB–TPA, and Py–TB–TPA.

Optical and electronic properties of TPA-linked CMPs

The ultraviolet-visible (UV-vis) absorption spectra were methodically measured for six different TPA–CMPs, as illustrated in Fig. 5a and b. It became evident that upon the introduction of a triple bond, TPA–TB–TPA, TPE–TB–TPA, and Py–TB–TPA CMPs displayed a pronounced redshift in the absorption onset towards higher wavelengths, resulting in enhanced absorption of visible light, as compared to their counterparts, TPA–TPA, TPE–TPA, and Py–TPA CMPs. Optical bandgap values were determined using Tauc plots, yielding 2.66 eV, 2.41 eV, and 2.10 eV for TPA–TPA, TPE–TPA, and Py–TPA CMPs, respectively [Fig. 5c]. Conversely, TPA–TB–TPA, TPE–TB–TPA, and Py–TB–TPA CMPs exhibited optical bandgap values of 2.01 eV, 2.29 eV, and 1.85 eV (Fig. 5d). The introduction of an acetylene group as π linker into TPA–TPA, TPE–TPA, and Py–TPA CMPs polymers resulted in a noticeable redshift in their absorption edges, enhancing their ability to absorb visible light. These findings emphasize the significant influence of acetylene group incorporation on the optical properties of these CMPs. Photoelectron spectroscopy was employed to determine the energy levels of polymers, with a specific emphasis on the highest occupied molecular orbital (HOMO) levels [Fig. 5e–l]. To ascertain the lowest unoccupied molecular orbital (LUMO) of the polymers, the following formula was utilized: $E_{HOMO} + E_g$, the resulting values are displayed in the provided Table 1. The HOMO values for TPA–TPA CMP, TPE–TPA CMP, Py–TPA CMP, TPA–TB–TPA CMP, TPE–TB–TPA CMP, and Py–TB–TPA CMP were found to be −5.31, −5.73, −5.59, −5.38, −5.61 and −5.55 eV; respectively [Fig. 5e–j]. As depicted in Fig. 5k and l, the LUMO levels of the polymers consistently surpassed the energy threshold necessary for water reduction, falling within the range of −2.65 eV to −3.70 eV. This suggests that these polymers have the potential to catalyze the hydrogen evolution reaction [Table 1]. To gain deeper insights into the intramolecular charge transfer characteristics of our CMPs, we investigated their photoluminescence properties.

As depicted in Fig. S35,† the photoluminescence spectra of synthesized CMPs with an alkyne linker exhibit a more pronounced red shift and enhanced photoluminescence quenching. This observation suggests a greater difficulty in the

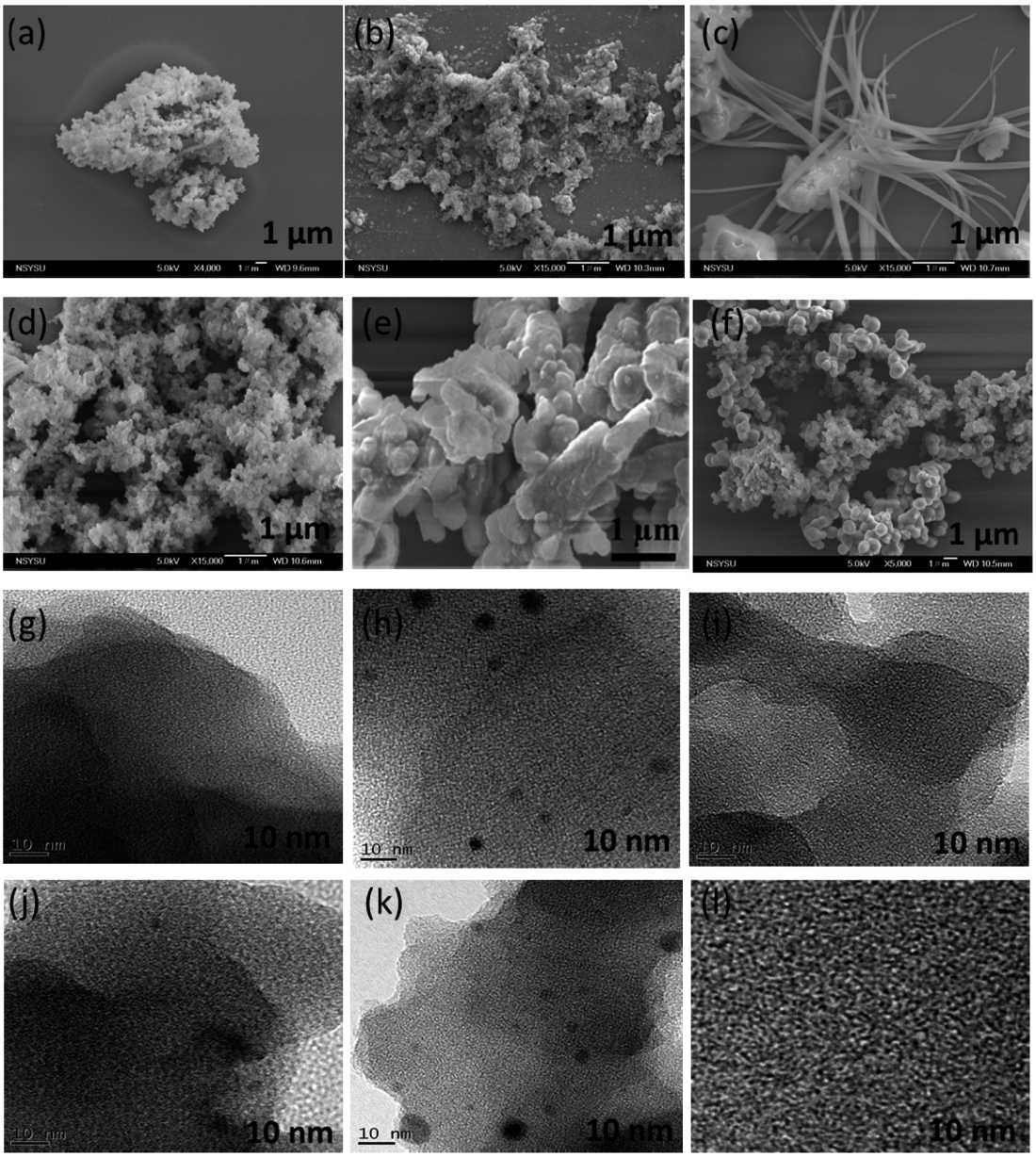

Fig. 4 SEM and TEM images of (a and g) TPA–TPA CMP, (b and h) TPE–TPA CMP, (c and i) Py–TPA CMP, (d and j) TPA–TB–TPA CMP, (e and k) TPE–TB–TPA CMP, and (f and l) Py–TB–TPA–CMP.

recombination of excitons through the radiative pathway, attributable to a heightened intramolecular charge transfer from the donor to acceptor segments compared to CMPs lacking the alkyne linker. This effect is attributed to the efficacious role of the alkyne linker, acting as a bridge between the donor and acceptor, thereby facilitating charge transfer and augmenting charge separation between them.

Photocatalytic hydrogen evolution of TPA–CMPs as a photocatalyst

We conducted a quantitative analysis of Pd residue utilizing Inductively Coupled Plasma Optical Emission Spectroscopy (ICP-OES). The findings are detailed in Table S2 of the ESI.† The ICP-OES results indicate that the Pd content (ppm) spans from 4.5 to 9 across all CMP materials. Notably, there is a negligible variance in Pd content among the different CMPs presented, suggesting a uniformity in the effect across materials. Consequently, it is reasonable to infer that this uniform effect is consistent across all materials concerning their photocatalytic activity for H_2 evolution. Moreover, the observed Pd content does not significantly impact the comparison between the various materials.[88,89] Following this, photocatalytic experiments were conducted to examine the generation of H_2 using TPA–CMP photocatalysts at room temperature. Visible light within the 380–780 nm range was used for irradiation. The gas produced in the photoreactor quantified at a rate of 500 μL per hour, was analyzed using gas chromatography. In the process of

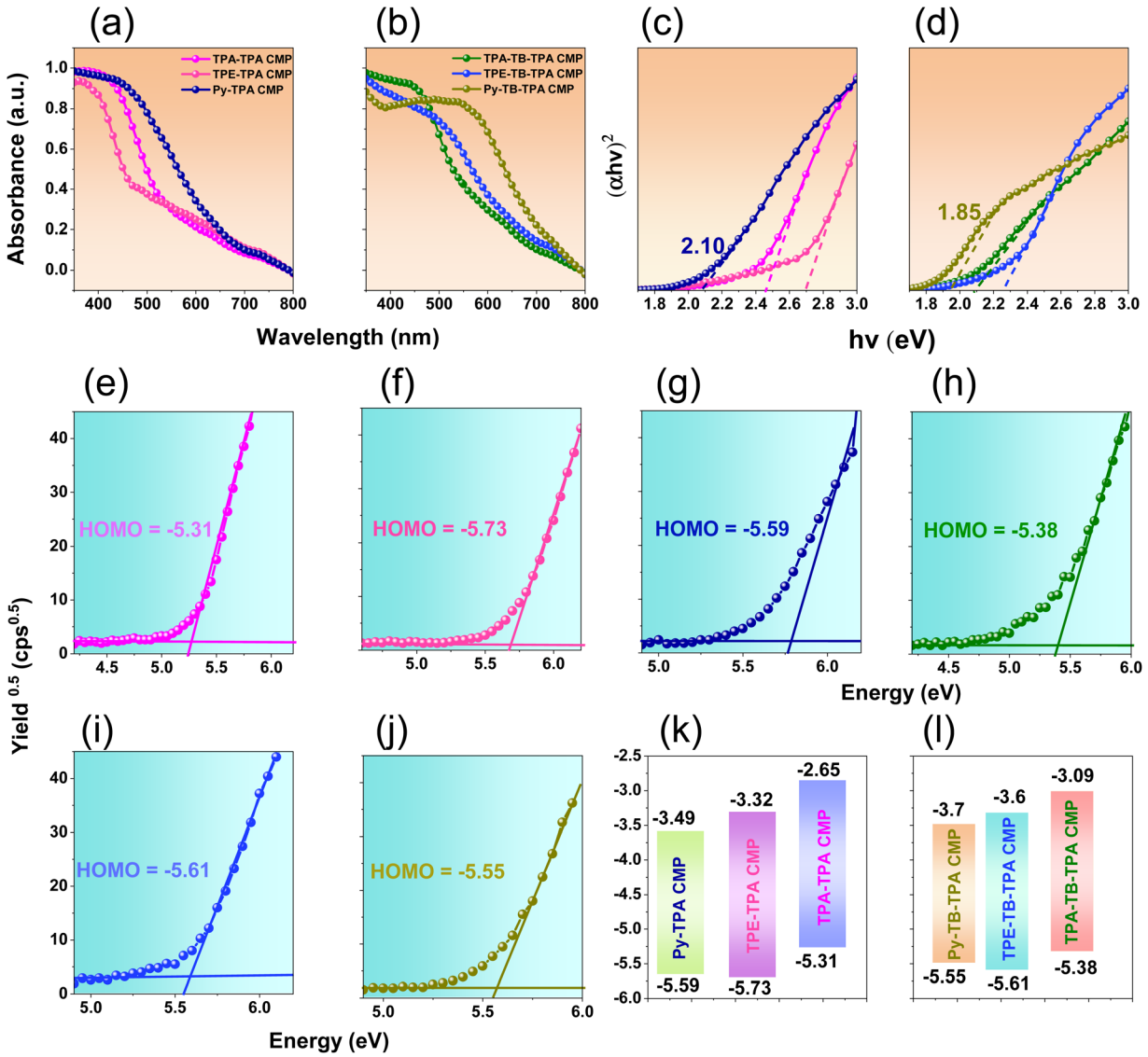

Fig. 5 (a and b) UV-vis absorption spectra, (c and d) the corresponding Tauc plots, (e–j) Photoelectron profiles, and (k and l) energy level diagram of the TPA-based CMPs photocatalysts.

Table 1 Photophysical properties and HER of the TPA-Linked CMPs

CMP	HOMO/LUMO (eV)	Bandgap (eV)	HER (μmol g^{-1} h^{-1})
TPA–TPA CMP	−5.31/−2.65	2.66	44
TPE–TPA CMP	−5.73/−3.32	2.41	109
Py–TPA CMP	−5.59/−3.49	2.10	3633
TPA–TB–TPA CMP	−5.38/−3.09	2.29	119
TPE–TB–TPA CMP	−5.61/−3.60	2.01	1107
Py–TB–TPA CMP	−5.55/−3.70	1.89	16 700

photocatalytic H_2 production from water, methanol was introduced to the polymers, and ascorbic acid (AA) served as a sacrificial electron donor (SED) to improve the dispersion of the photocatalyst in water. The photocatalytic hydrogen evolution rate (HER), in the absence of a platinum (Pt) co-catalyst, was determined to be 44, 109 μmol g^{-1} h^{-1}, and 3633 μmol g^{-1} h^{-1} for TPA–TPA TPE–TPA, and Py–TPA CMPs, respectively. In contrast, after the introduction of acetylene groups to these same polymers, the HER increased to 119 μmol g^{-1} h^{-1}, 1107 μmol g^{-1} h^{-1}, and 16 700 μmol g^{-1} h^{-1} for TPA–TB–TPA, TPE–TB–TPA, and Py–TB–TPA CMPs, respectively (Fig. 6a–c). These results highlight a significant improvement in photocatalytic hydrogen evolution associated with polymers containing acetylene groups, establishing them as highly effective photocatalysts in this regard.[77,81] Photocurrent analysis was conducted on these TPA-linked CMPs to gain insights into the charge transport mechanisms within these materials, as illustrated in Fig. 6d. Our investigation revealed that TPA–CMPs containing acetylene groups exhibited significantly higher photocurrents when compared to their counterparts without acetylene groups. This observation suggests that, when exposed to light, the electrons generated by incident light can be

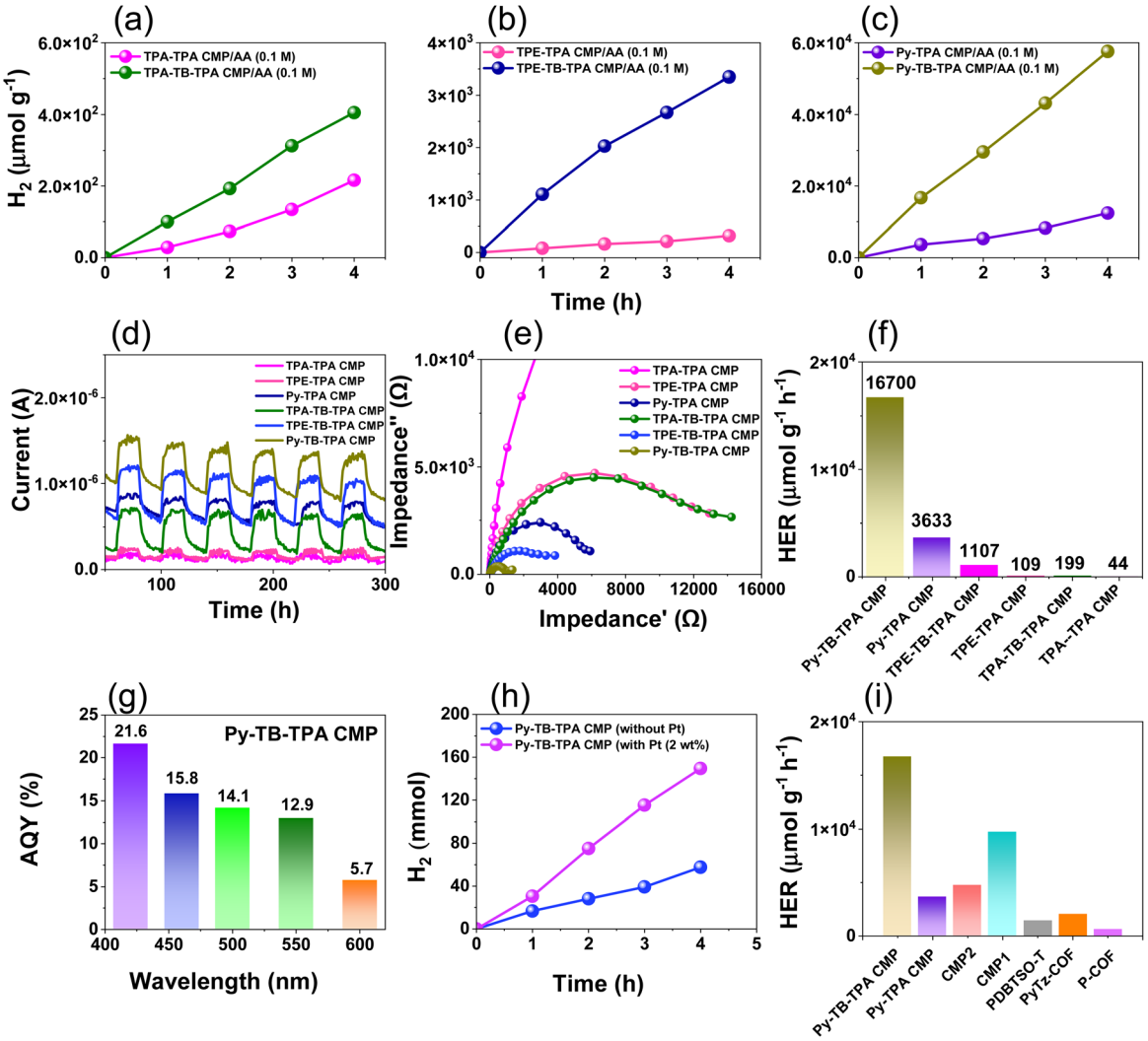

Fig. 6 The evolution of H_2 production over time for (a) TPA–TPA and TPA–TB–TPA CMPs, (b) TPE–TPA, and TPE–TB–TPA CMPs, and (c) Py–TPA and Py–TB–TPA CMPs in the presence of AA (0.1 M). The photocurrent (d) and (e) EIS and (f) HER profiles of TPA–TPA, TPE–TPA, Py–TPA, TPA–TB–TPA, TPE–TB–TPA, and Py–TB–TPA CMPs, (g) AQYs of the Py–TB–TPA CMP at various wavelengths of light in the presence of Pt, (h) HER profiles of Py–TB–TPA CMP in the presence of Pt and (i) the Py–TB–TPA CMP exhibited the highest HER values compared to other published materials.

efficiently separated and transported, with this effect being particularly pronounced in the acetylene-functionalized CMPs. To further assess the rate of charge transfer, electrochemical impedance spectroscopy (EIS) was utilized. As depicted in Fig. 6e, TPA–CMPs containing acetylene groups displayed EIS spectra with reduced intensity in comparison to TPA–CMPs without acetylene groups. This decrease in intensity indicates lower charge resistance in the former, emphasizing their superior charge transfer capabilities. The inclusion of an alkyne bridge in the Py–TB–TPA CMP is the key factor behind its elevated HER value (16 700 μmol g^{-1} h^{-1}) in contrast to the synthesized TPA–CMP samples in this investigation [Fig. 6f].[77,81] This bridge effectively inhibits the recombination of electron–hole pairs, extending the lifespan of charge carriers, and enhancing their transfer and separation efficiency, as visually demonstrated in Fig. 6f. This remarkable outcome underscores the potential of incorporating triple bonds to create highly efficient CMP photocatalysts. Under optimal conditions, the apparent quantum yield (AQY) of Py–TB–TPA CMP was assessed using monochromatic light at various wavelengths, including 420, 460, 500, 550, and 600 nm, to enhance the evaluation of its photocatalytic efficiency, as depicted in Fig. 6g and Table S3.† Remarkably, Py–TB–TPA CMP in the presence of Pt (2 wt%) surpassed previously reported CMPs, demonstrating an impressively high AQY of 21.6% at 420 nm. The platinum (Pt) source employed in this study was H_2PtCl_6. The highest HER was achieved by introducing a 2 wt% Pt co-catalyst to the Py–TB–TPA CMP solution, as depicted in Fig. 6h. Notably, the Py–TB–TPA CMP exhibited an exceptional HER of approximately 44 300 μmol g^{-1} h^{-1} [Fig. 6h and S36†]. Fig. S37† illustrates the sustained hydrogen evolution reaction (HER) observed in Py–TB–TPA CMP for a duration exceeding 20 hours, with no discernible

deterioration. The photocatalytic efficacy of the material remained consistently stable throughout the entire duration. The resilience demonstrated by this polymer photocatalyst holds promise for practical applications in real-world scenarios, showcasing its potential suitability for extended use. In contrast to other published materials, Fig. 6i demonstrates that the Py–TB–TPA CMP exhibited the highest HER values. Table S4† provides a summary of the photocatalytic performance of our synthetic TPA–CMPs and TPA–TB–CMPs materials for hydrogen evolution, comparing them to other reported materials.

Computational methodology of TPA–CMP samples

In this study, all computational calculations for the molecules under investigation were conducted using the Density Functional Theory (DFT) method with Gaussian 16 revision A.03 software.[90] Subsequently, the obtained results were visualized using GaussView 5 software.[91] Ground state geometry optimization and vibrational frequency calculations for the designed molecules were performed using DFT with the B3LYP method[92,93] and a 6-31G (d) basis set. The absence of negative vibrational modes in the optimized structures confirms that they are situated at a minimum potential energy state. To explore the excited state properties and predict UV-vis absorption spectra, Time-Dependent Density Functional Theory (TD-DFT) methods were employed.[94] Electronic and optical properties of the molecules in a solvent phase (methanol) were determined for the optimized structures using the TD-B3LYP/6-31G(d) level of theory. Additionally, we assessed the significant contributions of molecular orbitals to electronic absorption bands by employing the GaussSum 3.0 program.[95] To understand the chemical reactivities of these CMPs, reactivity indices were derived from the Highest Occupied Molecular Orbital (HOMO) and Lowest Unoccupied Molecular Orbital (LUMO) energy eigenvalues.[96] Furthermore, we presented Molecular Electrostatic Potential (MEP) plots to identify potential sites for electrophilic and nucleophilic attacks on the compounds. The frontier molecular orbitals (FMOs) study offers prospective explanations of electron delocalization and electron transfer capabilities inside the molecule.[97] As part of our investigation into how donor and acceptor fragments affect the photoelectric properties of the studied compounds, the HOMO and LUMO energy levels, the bandgap, and the chemical reactivity indices were investigated using the DFT calculations and listed in Table S5.† The FMOs (Fig. 7) were conducted at optimized ground-state geometries.

As demonstrated in Fig. 7a, for Py–TPA, TPA–TPA, and TPE–TPA CMPs, the HOMOs were mainly distributed on the triphenylamine donor and slightly spread over the acceptor part while LUMOs were distributed on the acceptor portions.[98,99] These distributions indicate high electron delocalization and important charge transfer (CT) occurs inside the investigated compounds under light irradiation. The donor–π–donor (D–π–D) and donor–π–acceptor (A–π–D) polymers (TPA–TB–TPA, TPE–TB–TPA, and Py–TB–TPA CMPs) also exhibit similar behavior [Fig. 7a]. Nevertheless, alkynyl (π-bridges) also donate some charges to the HOMOs; also, partial electrons may remain on the alkynyl moieties in the LUMOs.[100] Both HOMO and LUMO exhibit significant overlaps on the π-bridge group, resulting in advantageous spatial distributions for the intramolecular charge transfer process. The Py–TB–TPA CMP had a significantly smaller HOMO–LUMO energy gap than other polymers, indicating that it has superior CT and red-shifted absorption. As seen in Fig. 7b and c, the difference in charge density between the excited and ground states makes it possible to view the intramolecular charge transfer process. The charge density difference HOMOs and LUMOs. The bandgap energy is the most critical factor in the photocatalytic process since it offers valuable information for charge transfer. In general, the bandgap affects the transfer of electrons from HOMO to LUMO by absorbing light energy of the appropriate wavelength.[101] The predicted energy gaps (Fig. 7a and Table S5†) of the investigated compounds decrease in the following order: TPA–TPA > TPE–TB–TPA > TPE–TPA > TPA–TB–TPA > Py–TPA > Py–TB–TPA CMP. The results indicate that Py–TB–TPA CMP has lower bandgap energy than other compounds. Therefore, the transition from HOMO to LUMO can occur rapidly. Consequently, it is suggested that Py–TB–TPA CMP should be a successful candidate for H_2 evolution, whereas TPA–TPA CMP will be more stable due to its larger energy gap (Fig. 7), which is in good agreement with the experimental findings. We observed that the inclusion of alkynyl π-bridges slightly stabilized the HOMO/LUMO, resulting in a narrowing bandgap (E_g), which facilitates electron transfer from HOMOs to LUMOs, thus enhancing the photocatalytic activity. By utilizing molecular electrostatic potential (MEP) analysis, we were able to identify the exact reactive sites inside the molecules.[102] The red-colored area on the MEP surface map represents the electron acceptor region, whereas the blue-colored area represents the electron donor in the molecule. The potential increases in the order red < orange < yellow < green < blue. Fig. 7f displays the electrostatic potential characteristics through plots for Py–TB–TPA CMP. The TPA part of Py–TB–TPA CMP works as the electron donor and has a positive electron potential. The pyrene moiety in Py–TB–TPA CMP works as the electron acceptor and has a negative electron potential. The chemical reactivity parameters can be used to analyze the photoelectric properties of molecules. The chemical reactivity parameters, such as ionization potential (I), electron affinity (A), electronegativity (χ), absolute hardness (η), and softness (S), were calculated based on the HOMO and LUMO energy levels of the investigated compounds (Table S5†). It is not easy to polarize a molecule with a large energy gap since it requires more excitation energy. In contrast, a molecule with a small energy gap can easily polarize and be relatively more reactive than chemically hard molecules because it can easily donate electrons to an acceptor. The studied compounds were subjected to a comparative analysis of the global reactivity descriptors (Table S5†). The Py–TB–TPA CMP has the lowest chemical hardness value (1.42 eV) among the other compounds. On the other side, the electronegativity factor identified the chemical behavior of the molecule. The higher value of the electronegativity (3.49 eV) reflects the chemical activity of the Py–TB–TPA CMP. The chemical reactivity descriptors reveal that Py–TB–TPA CMP is the most chemically reactive (soft)

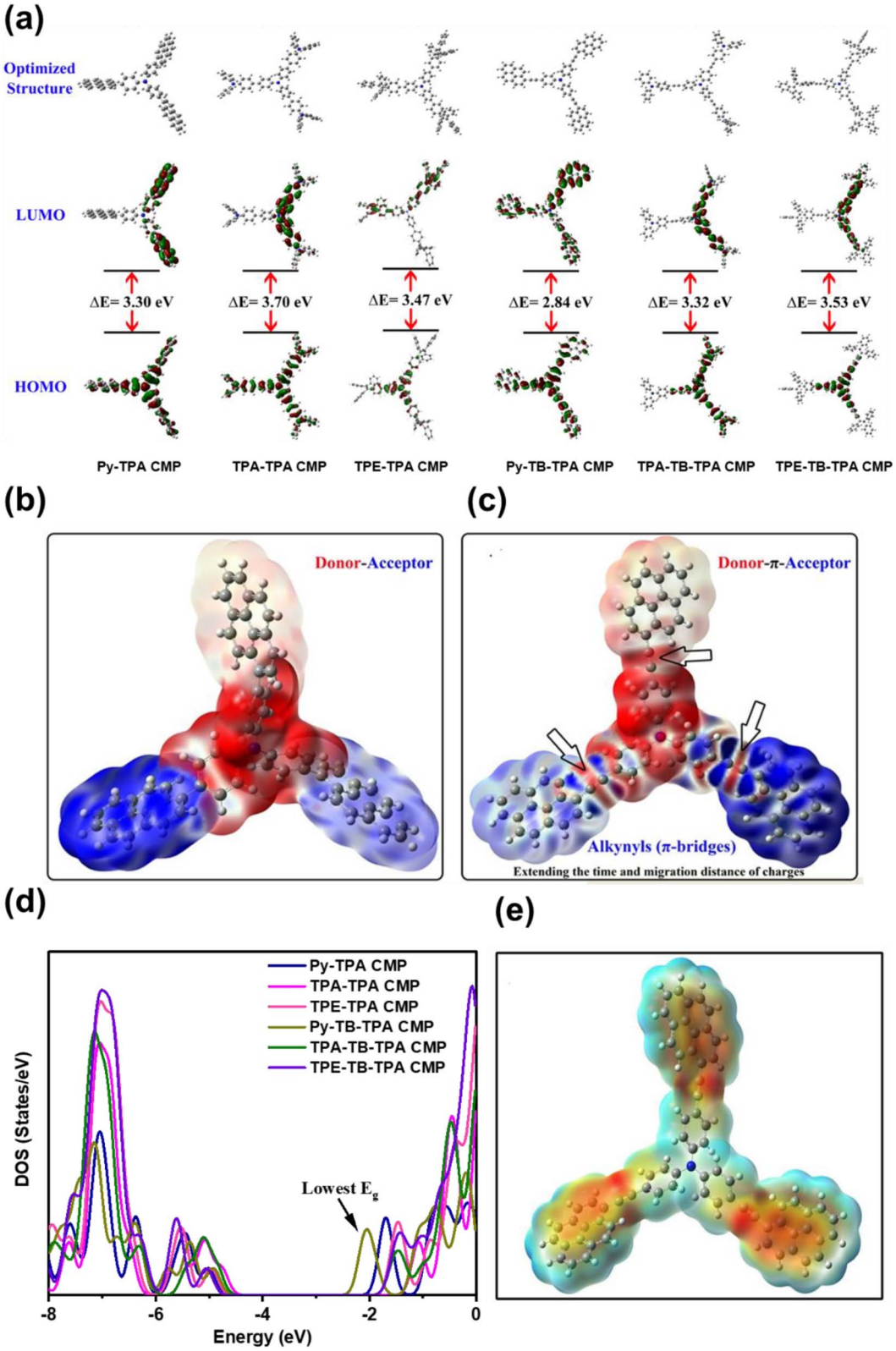

Fig. 7 (a) Optimized geometries, frontier molecular orbital contour plots with HOMO–LUMO gaps of the Py–TPA, TPA–TPA, TPE–TPA, Py–TB–TPA, TPA–TB–TPA, and TPE–TB–TPA CMPs, the charge density difference between the excited and ground states of (b) Py–TPA and (c) Py–TB–TPA CMPs. (d) The density of states (DOS) of the studied TPA-linked CMPs and (e) molecular electrostatic potential (MEP) of Py–TB–TPA CMP.

compound and may reduce charge transfer resistance compared to the other compounds, suggesting that this compound has the best photoelectric properties. The cost-effective TD-DFT method was used to estimate the optical properties of the studied molecules and to investigate the impact of the π-conjugated bridge on the absorption spectra.[103] In the MeOH solvent phase, the optical absorption spectra were simulated using the TD-DFT/B3LYP/6-311 g(d,p) level. As shown in Fig. S38,† all the investigated compounds display a maximum absorption band between 300 and 600 nm, covering a significant part of the solar spectrum. Compared to other polymers, we observed a redshift in the polymer containing the π-linker, indicating that the π-linker improves the electron delocalization and optical properties. As demonstrated in Fig. S38,† the Py–TB–TPA CMP has a maximum wavelength of 498 nm, which is longer than other molecules. The absorption peak red shifted in Py–TB–TPA CMP because of the decreased HOMO–LUMO gap. There is a correlation between the simulated and experimental spectra, demonstrating that the utilized theoretical method is reliable.

Conclusions

To summarize, six different CMPs [(D–D), (D–π–D), and (A–π–D)] were created by coupling alkyne groups with triphenylamine (TPA) for photocatalytic H_2 evolution from H_2O. These CMPs were synthesized using Suzuki and Sonogashira–Hagihara coupling reactions. The following CMP materials were generated: TPA–TPA, TPE–TPA, Py–TPA, TPA–TB–TPA, TPE–TB–TPA, and Py–TB–TPA CMPs. Among these CMPs, TPA–TPA CMP exhibited a T_{d10} value of 557 °C, while Py–TPA CMP and TPA–TB–TPA CMP displayed high thermal decomposition temperatures of 508 °C and 482 °C, respectively. Py–TPA and Py–TB–TPA CMPs exhibited significant HER of 3633 and 16 700 μmol g^{-1} h^{-1}, respectively, in the context of photocatalytic H_2 production. DFT calculations indicated that the Py–TB–TPA CMP, featuring an alkyne bridge, effectively mitigated electron–hole recombination, prolonging the lifetime of charge carriers while enhancing their transfer and separation efficiency. This stood in contrast to a similar CMP (Py–TPA CMP) lacking an alkynyl group. The addition of the alkynyl bridge notably increased the polymers' photocatalytic activity. This study underscores the potential applications of high-performance CMPs incorporating alkynyl groups in photocatalysis, providing insights into their design and synthesis from various angles.

Author contributions

Mohamed Gamal Mohamed: investigation, methodology, conceptualization, supervision, writing – original draft. Mohamed Hammad Elsayed: investigation, methodology. Chia-Jung Li: investigation. Ahmed E. Hassan: investigation, methodology. Islam M. A. Mekhemer: investigation. Ahmed Fouad Musa: investigation. Mahmoud Kamal Hussien: investigation. Li-Chyong Chen: supervision. Kuei-Hsien Chen: supervision. Ho-Hsiu Chou: supervision. Shiao-Wei Kuo: supervision.

Conflicts of interest

There are no conflicts to declare.

Acknowledgements

This study was supported financially by the Ministry of Science and Technology, Taiwan, under contracts MOST 108-2638-E-002-003-MY2, and 108-2221-E-110-014-MY3. The authors thank the staff at National Sun Yat-sen University for their assistance with TEM (ID: EM022600) experiments.

Notes and references

1 C. Yang, C. Qian, M. Yu and Y. Liao, Manipulation of band gap and hydrophilicity in vinylene-linked covalent organic frameworks for improved visible-light-driven hydrogen evolution by end-capping strategy, *Chem. Eng. J.*, 2023, **454**, 140341, DOI: 10.1016/j.cej.2022.140341.

2 M. M. Samy, I. M. A. Mekhemer, M. G. Mohamed, M. H. Elsayed, K. H. Lin, Y. K. Chen, T. L. Wu, H. H. Chou and S. W. Kuo, Conjugated microporous polymers incorporating Thiazolo[5,4-d]thiazole moieties for Sunlight-Driven hydrogen production from water, *Chem. Eng. J.*, 2022, **446**, 137158, DOI: 10.1016/j.cej.2022.137158.

3 Z. Ajmal, A. Qadeer, U. Khan, M. B. Hussain, M. Irfan, M. Abid, R. Djellabi, A. Kumar, H. Ali, A. Kalam, H. Algarni, Y. Al-Hadeethi, J. Qian, A. Hayat and H. Zeng, Current progresses in two-dimensional MXene-based framework: prospects from superficial synthesis to energy conversion and storage applications, *Mater. Today Chem.*, 2023, **27**, 101238, DOI: 10.1016/j.mtchem.2022.101238.

4 J. Chen, B. Liu, H. Cai, S. Liu, Y. Yamauchi and S. C. Jun, Covalently Interlayer-Confined Organic–Inorganic Heterostructures for Aqueous Potassium Ion Supercapacitors, *Small*, 2023, **19**, 2204275, DOI: 10.1002/smll.202204275.

5 M. G. Mohamed, M. H. Elsayed, Y. Ye, M. M. Samy, A. E. Hassan, T. H. Mansoure, Z. Wen, H. H. Chou, K. H. Chen and S. W. Kuo, Construction of Porous Organic/Inorganic Hybrid Polymers Based on Polyhedral Oligomeric Silsesquioxane for Energy Storage and Hydrogen Production from Water, *Polymers*, 2023, **15**, 182, DOI: 10.3390/polym15010182.

6 A. O. Mousa, M. G. Mohamed, C. H. Chuang and S. W. Kuo, Carbonized Aminal-Linked Porous Organic Polymers Containing Pyrene and Triazine Units for Gas Uptake and Energy Storage, *Polymers*, 2023, **15**, 1891, DOI: 10.3390/polym15081891.

7 K. Chang, D. T. Tran, J. Wang, K. Dong, S. Prabhakaran, D. H. Kim, N. H. Kim and J. H. Lee, Triphasic Ni_2P–Fe_2P–CoP heterostructure interfaces for efficient overall water splitting powered by solar energy, *Appl. Catal., B*, 2023, **338**, 123016, DOI: 10.1016/j.apcatb.2023.123016.

8 M. G. Mohamed, S. Y. Chang, M. Ejaz, M. M. Samy, A. O. Mousa and S. W. Kuo, Design and Synthesis of

Bisulfone-Linked Two-Dimensional Conjugated Microporous Polymers for CO_2 Adsorption and Energy Storage, *Molecules*, 2023, **28**, 3234, DOI: 10.3390/molecules28073234.

9 M. M. Samy, M. G. Mohamed, S. U. Sharma, S. V. Chaganti, T. H. Mansoure, J. T. Lee, T. Chen and S. W. Kuo, Constructing conjugated microporous polymers containing triphenylamine moieties for high-performance capacitive energy storage, *Polymer*, 2023, **264**, 125541, DOI: 10.1016/j.polymer.2022.125541.

10 L. Chai, S. Liu, S. Pei and C. Wang, Electrodeposited amorphous cobalt-nickel-phosphide-derived films as catalysts for electrochemical overall water splitting, *Chem. Eng. J.*, 2021, **420**, 129686, DOI: 10.1016/j.cej.2021.129686.

11 M. M. Samy, M. G. Mohamed and S. W. Kuo, Pyrene-functionalized tetraphenylethylene polybenzoxazine for dispersing single-walled carbon nanotubes and energy storage, *Compos. Sci. Technol.*, 2020, **199**, 108360, DOI: 10.1016/j.compscitech.2020.108360.

12 C. Yang, C. Qian, M. Yu and Y. Liao, Manipulation of band gap and hydrophilicity in vinylene-linked covalent organic frameworks for improved visible-light-driven hydrogen evolution by end-capping strategy, *J. Chem. Eng.*, 2023, **454**, 140341, DOI: 10.1016/j.cej.2022.140341.

13 A. Meng, H. Zhang, B. Huangfu, W. Tian, L. Sheng, Z. Li, S. Tan and Q. Li, Bimetal nickel–cobalt phosphide directly grown on commercial graphite substrate by the one-step electrodeposition as efficient electrocatalytic electrode, *Prog. Nat. Sci.: Mater. Int.*, 2020, **30**, 461–468, DOI: 10.1016/j.pnsc.2020.08.003.

14 J. Su, J. Zhou, L. Wang, C. Liu and Y. Chen, Synthesis and application of transition metal phosphides as electrocatalyst for water splitting, *Sci. Bull.*, 2017, **62**, 633–644, DOI: 10.1016/j.scib.2016.12.011.

15 R. R. Beswick, A. M. Oliveira and Y. Yan, Does the Green Hydrogen Economy Have a Water Problem?, *ACS Energy Lett.*, 2021, **6**, 3167–3169, DOI: 10.1021/acsenergylett.1c01375.

16 A. M. Oliveira, R. R. Beswick and Y. Yan, A Green Hydrogen Economy for a Renewable Energy Society, *Curr. Opin. Chem. Eng.*, 2021, **33**, 100701, DOI: 10.1016/j.coche.2021.100701.

17 M. E. Webber, The Water Intensity of the Transitional Hydrogen Economy, *Environ. Res. Lett.*, 2007, **2**, 229–269, DOI: 10.1088/1748-9326/2/3/034007.

18 M. A. Khan, T. A. Al-Attas, S. Roy, M. M. Rahman, N. Ghaffour, V. Thangadurai, S. Larter, J. Hu, P. Ajayan and M. G. Kibria, Seawater Electrolysis for Hydrogen Production: A Solution Looking for a Problem?, *Energy Environ. Sci.*, 2021, **9**, 1–16, DOI: 10.1039/D1EE00870F.

19 P. Woods, H. Bustamante and K. F. Aguey-Zinsou, The hydrogen economy-Where is the water?, *Energy Nexus*, 2022, **7**, 100123, DOI: 10.1016/j.nexus.2022.100123.

20 N. Rambhujun, M. S. Salman, T. Wang, C. Pratthana, P. Sapkota, M. Costalin, Q. Lai and K. F. Aguey-Zinsou, Renewable hydrogen for the chemical industry, *MRS Energy Sustain.*, 2020, **7**, E33, DOI: 10.1557/mre.2020.33.

21 S. Sharma, S. Basu, N. P. Shetti and T. M. Aminabhavi, Waste-to-energy nexus for circular economy and environmental protection: recent trends in hydrogen energy, *Sci. Total Environ.*, 2020, **713**, 136633, DOI: 10.1016/j.scitotenv.2020.136633.

22 M. Gao, C. K. Peh, L. Zhu, G. Yilmaz and G. W. Ho, Photothermal catalytic gel featuring spectral and thermal management for parallel freshwater and hydrogen production, *Adv. Energy Mater.*, 2020, **10**, 2000925, DOI: 10.1002/aenm.202000925.

23 A. E. Hassan, M. H. Elsayed, M. S. A. Hussien, M. G. Mohamed, S. W. Kuo, H. H. Chou, I. S. Yahia, T. A. Mohamed and Z. Wen, V_2O_5 nanoribbons/N-deficient g-C_3N_4 heterostructure for enhanced visible-light photocatalytic performance, *Int. J. Hydrogen Energy*, 2023, **48**, 9620–9635, DOI: 10.1016/j.ijhydene.2022.12.009.

24 J.-H. Zhang, M.-J. Wei, Z.-W. Wei, M. Pan and C.-Y. Su, Ultrathin Graphitic Carbon Nitride Nanosheets for Photocatalytic Hydrogen Evolution, *ACS Appl. Nano Mater.*, 2020, **3**, 1010–1018, DOI: 10.1021/acsanm.9b02590.

25 P. Niu, M. Qiao, Y. Li, L. Huang and T. Zhai, Distinctive defects engineering in graphitic carbon nitride for greatly extended visible light photocatalytic hydrogen evolution, *Nano Energy*, 2018, **44**, 73–81, DOI: 10.1016/j.nanoen.2017.11.059.

26 L. Zhang, Z. Jin, S. Huang, X. Huang, B. Xu, L. Hu, H. Cui, S. Ruan and Y.-J. Zeng, Bio-inspired carbon doped graphitic carbon nitride with booming photocatalytic hydrogen evolution, *Appl. Catal., B*, 2019, **246**, 61–71, DOI: 10.1016/j.apcatb.2019.01.040.

27 M. Liu, Z. Yao, J. Gu, C. Li, X. Huang, L. Zhang, Z. Huang and M. Fan, Issues and opportunities facing hydrolytic hydrogen production materials, *Chem. Eng. J.*, 2023, **461**, 141918, DOI: 10.1016/j.cej.2023.141918.

28 F. E. Osterloh, Inorganic Materials as Catalysts for Photochemical Splitting of Water, *Chem. Mater.*, 2008, **20**, 35–54, DOI: 10.1021/cm7024203.

29 X. Li, Y. Chen, Y. Tao, L. Shen, Z. Xu, Z. Bian and H. Li, Challenges of photocatalysis and their coping strategies, *Chem Catal.*, 2022, **2**, 1315–1345, DOI: 10.1016/j.checat.2022.04.007.

30 Y. Wang, A. Vogel, M. Sachs, R. S. Sprick, L. Wilbraham, S. J. A. Moniz, R. Godin, M. A. Zwijnenburg, J. R. Durrant, A. I. Cooper and J. Tang, Current understanding and challenges of solar-driven hydrogen generation using polymeric photocatalysts, *Nat. Energy*, 2019, **4**, 746–760, DOI: 10.1038/s41560-019-0456-5.

31 A. E Hassan, M. S. A. Hussien, M. H. Elsayed, M. G. Mohamed, S. W. Kuo, H. H. Chou, I. S Yahia, G. Wang and Z. Wen, One-step construction of Y, C, and O tridoped g-C_3N_4 as a bifunctional photocatalyst for H_2 evolution and organic pollutant degradation under visible light irradiation, *Sustainable Energy Fuels*, 2022, **6**, 3858–3871, DOI: 10.1039/D2SE00525E.

32 M. H. Elsayed, M. Abdellah, A. Z. Alhakemy, I. M. A. Mekhemer, A. E. A. Aboubakr, B. H. Chen, A. Sabbah, K. H. Lin, W. S. Chiu, S. J. Lin, C. Y. Chu,

C. H. Lu, S. D. Yang, M. G. Mohamed, S. W. Kuo, C. H. Hung, L. C. Chen, K. H. Chen and H. H. Chou, Overcoming small-bandgap charge recombination in visible and NIR-light-driven hydrogen evolution by engineering the polymer photocatalyst structure, *Nat. Commun.*, 2024, **15**, 707, DOI: **10.1038/s41467-024-45085-6**.

33 B. Chen, N. Yang, P. Wang, Y. Xiang and H. Chen, Post-side chain engineering of difluorinated benzothiadiazole-based conjugated microporous polymer for enhanced photocatalytic H_2 evolution, *Appl. Surf. Sci.*, 2020, **499**, 143865, DOI: **10.1016/j.apsusc.2019.143865**.

34 M. G. Mohamed, M. H. Elsayed, A. M. Elewa, A. F. M. EL-Mahdy, C.-H. Yang, A. A. Mohammed, H.-H. Chou and S.-W. Kuo, Pyrene-containing conjugated organic microporous polymers for photocatalytic hydrogen evolution from water, *Catal. Sci. Technol.*, 2021, **11**, 2229–2241, DOI: **10.1039/D0CY02482A**.

35 L. Wang, Y. Wan, Y. Ding, S. Wu, Y. Zhang, X. Zhang, G. Zhang, Y. Xiong, X. Wu and J. Yang, Conjugated microporous polymer nanosheets for overall water splitting using visible light, *Adv. Mater.*, 2017, **29**, 1702428, DOI: **10.1002/adma.201702428**.

36 S. Xiang, C. Han, C. Shu, C. Zhang and J.-X. Jiang, Structure evolution of thiophene-containing conjugated polymer photocatalysts for high-efficiency photocatalytic hydrogen production, *Sci. China Mater.*, 2022, **65**, 422–430, DOI: **10.1007/s40843-021-1757-1**.

37 S. Y. Chang, A. M. Elewa, M. G. Mohamed, I. M. A. Mekhemer, M. M. Samy, K. Zhang, H.-H. Chou and S. W. Kuo, Rational design and synthesis of bifunctional Dibenzo[g,p]chrysene-based conjugated microporous polymers for energy storage and visible light-driven photocatalytic hydrogen evolution, *Mater. Today Chem.*, 2023, **33**, 101680, DOI: **10.1016/j.mtchem.2023.101680**.

38 W. T. Chung, I. M. A. Mekhemer, M. G. Mohamed, A. M. Elewa, A. F. M. EL-Mahdy, H. H. Chou, S. W. Kuo and K. C. W. Wu, Recent advances in metal/covalent organic frameworks based materials: Their synthesis, structure design and potential applications for hydrogen production, *Coord. Chem. Rev.*, 2023, **483**, 215066, DOI: **10.1016/j.ccr.2023.215066**.

39 W. He, J. Zhou, W. Xu, C. Li, J. Li and N. Wang, Regulating the Content of Donor Unit in Donor–Acceptor Covalent Triazine Frameworks for Promoting Photocatalytic H_2 Production, *ChemSusChem*, 2023, e202301175, DOI: **10.1002/cssc.202301175**.

40 W. Huang, Q. He, Y. Hu and Y. Li, Molecular Heterostructures of Covalent Triazine Frameworks for Enhanced Photocatalytic Hydrogen Production, *Angew. Chem., Int. Ed.*, 2019, **58**, 8676–8680.

41 M. Chen, J. Xiong, Q. Shi, T. Li, X. Li, Y. Feng and B. Zhang, How the π bridge in donor–π–acceptor type covalent triazine frameworks influenced their photocatalytic hydrogen evolution performance, *Chem. Eng. J.*, 2023, **475**, 146099, DOI: **10.1016/j.cej.2023.146099**.

42 A. Liu, S. Wang, H. Song, Y. Liu, L. Gedda, K. Edwards, L. Hammarström and H. Tian, Excited-state and charge-carrier dynamics in binary conjugated polymer dots towards efficient photocatalytic hydrogen evolution, *Phys. Chem. Chem. Phys.*, 2023, **25**, 2935–2945, DOI: **10.1039/D2CP04204E**.

43 L. Ding, Z. N. Li, R. Y. Liu, Y. F. Li, G. D. Yang, Z. H. Kang, B. Yang, M. X. Deng and H. Z. Sun, Fabrication of electron's path based on carbonized polymer dots to accelerate photocatalytic hydrogen production kinetic for carbon nitride, *Appl. Catal., B*, 2023, **334**, 122806, DOI: **10.1016/j.apcatb.2023.122806**.

44 Y. Shi, A. F. Yang, C. S. Cao and B. Zhao, Applications of MOFs: Recent advances in photocatalytic hydrogen production from water, *Coord. Chem. Rev.*, 2019, **390**, 50–75, DOI: **10.1016/j.ccr.2019.03.012**.

45 M. Chen, K. Umer, B. Li, Z. Li, K. Li, W. Sun and Y. Ding, Metalloporphyrin based MOF-545 coupled with solid solution ZnxCd1-xS for efficient photocatalytic hydrogen production, *J. Colloid Interface Sci.*, 2024, **653**, 380–389, DOI: **10.1016/j.jcis.2023.09.080**.

46 J. J. Jiang, F. J. Zhang and Y. R. Wang, Review of different series of MOF/g-C_3N_4 composites for photocatalytic hydrogen production and CO_2 reduction, *New J. Chem.*, 2023, **47**, 1599–1609, DOI: **10.1039/D2NJ05260A**.

47 P. N. Singh, M. G. Mohamed, S. V. Chaganti, S. U. Sharma, M. Ejaz, J. T. Lee and S. W. Kuo, Rational Design of Ultrastable Conjugated Microporous Polymers based on Pyrene and Perylene Units as High-Performance Organic Electrode Materials for Supercapacitor Applications, *ACS Appl. Energy Mater.*, 2023, **6**, 8277–8287, DOI: **10.1021/acsaem.3c01391**.

48 M. G. Mohamed, H. Y. Hu, M. Madhu, M. M. Samy, I. M. A. Mekhemer, W. L. Tseng, H. H. Chou and S. W. Kuo, Ultrastable two-dimensional fluorescent conjugated microporous polymers containing pyrene and fluorene units for metal ion sensing and energy storage, *Eur. Polym. J.*, 2023, **189**, 111980, DOI: **10.1016/j.eurpolymj.2023.111980**.

49 T. H. Weng, M. G. Mohamed, S. U. Sharma, S. V. Chaganti, M. M. Samy, J. T. Lee and S. W. Kuo, Ultrastable Three-Dimensional Triptycene- and Tetraphenylethene-Conjugated Microporous Polymers for Energy Storage, *ACS Appl. Energy Mater.*, 2022, **5**, 14239–14249, DOI: **10.1021/acsaem.2c02809**.

50 M. G. Mohamed, M. M. Samy, T. H. Mansoure, C. J. Li, W. C. Li, J. H. Chen, K. Zhang and S. W. Kuo, Microporous Carbon and Carbon/Metal Composite Materials Derived from Bio-Benzoxazine-Linked Precursor for CO_2 Capture and Energy Storage Applications, *Int. J. Mol. Sci.*, 2022, **23**, 347, DOI: **10.3390/ijms23010347**.

51 W. Zhang, S. Li, X. Tang, J. Tang, C. Pan and G. Yu, Phenothiazine core promoted charge transfer in conjugated microporous polymers for photocatalytic Ugi-type reaction and aerobic selenation of indoles, *Appl. Catal., B*, 2020, **272**, 118982, DOI: **10.1016/j.apcatb.2020.118982**.

52 Q. Xie, Y. Yang, W. Zhang, Z. Gao, X. Li, J. Tang, C. Pana and G. Yu, Polarization-induced charge separation in conjugated microporous polymers for efficient visible light-driven C-3 selenocyanation of indoles, *Chem. Sci.*, 2021, **12**, 5631–5637, DOI: **10.1039/D0SC06951E**.

53 M. Ejaz, M. G. Mohamed and S. W. Kuo, Solid-state chemical transformation provides a fully benzoxazine-linked porous organic polymer displaying enhanced CO_2 capture and supercapacitor performance, *Polym. Chem.*, 2023, **14**, 2494–2509, DOI: **10.1039/D3PY00158J**.

54 J. S. M. Lee and A. I. Cooper, Advances in Conjugated Microporous Polymers, *Chem. Rev.*, 2020, **120**, 2171–2214, DOI: **10.1021/acs.chemrev.9b00399**.

55 M. G. Mohamed, E. C. Atayde, B. M. Matsagar, J. Na, Y. Yamauchi, K. C. W. Wu and S. W. Kuo, Construction Hierarchically Mesoporous/Microporous Materials Based on Block Copolymer and Covalent Organic Framework, *J. Taiwan Inst. Chem. Eng.*, 2020, **112**, 180–192, DOI: **10.1016/j.jtice.2020.06.013**.

56 Y. S. Ye, M. G. Mohamed and S. W. Kuo, Integrating the multiple functionalities in metalloporphyrin porous organic polymers enabling strong polysulfide anchoring and rapid electrochemical kinetics in Li–S batteries, *J. Mater. Chem. A*, 2023, **11**, 9112–9124, DOI: **10.1039/D2TA09232H**.

57 M. G. Mohamed, A. F. M. EL-Mahdy, M. G. Kotp and S. W. Kuo, Advances in porous organic polymers: syntheses, structures, and diverse applications, *Adv. Mater.*, 2022, **3**, 707–733, DOI: **10.1039/D1MA00771H**.

58 M. Ejaz, M. M. Samy, Y. Ye, S. W. Kuo and M. G. Mohamed, Design Hybrid Porous Organic/Inorganic Polymers Containing Polyhedral Oligomeric Silsesquioxane/Pyrene/Anthracene Moieties as a High-Performance Electrode for Supercapacitor, *Int. J. Mol. Sci.*, 2023, **24**, 2501, DOI: **10.3390/ijms24032501**.

59 M. M. Samy, M. G. Mohamed, S. U. Sharma, S. V. Chaganti, J. T. Lee and S. W. Kuo, An Ultrastable Tetrabenzonaphthalene-Linked conjugated microporous polymer functioning as a high-performance electrode for supercapacitors, *J. Taiwan Inst. Chem. Eng.*, 2023, 104750, DOI: **10.1016/j.jtice.2023.104750**.

60 M. G. Mohamed, S. U. Sharma, N. Y. Liu, T. H. Mansoure, M. M. Samy, S. V. Chaganti, Y. L. Chang, J. T. Lee and S. W. Kuo, Ultrastable Covalent Triazine Organic Framework Based on Anthracene Moiety as Platform for High-Performance Carbon Dioxide Adsorption and Supercapacitors, *Int. J. Mol. Sci.*, 2022, **23**, 3174, DOI: **10.3390/ijms23063174**.

61 A. O. Mousa, M. G. Mohamed, C. H. Chuang and S. W. Kuo, Carbonized Aminal-Linked Porous Organic Polymers Containing Pyrene and Triazine Units for Gas Uptake and Energy Storage, *Polymers*, 2023, **15**, 1891, DOI: **10.3390/polym15081891**.

62 R. S. Sprick, Y. Bai, A. A. Y. Guilbert, M. Zbiri, C. M. Aitchison, L. Wilbraham, Y. Yan, D. J. Woods, M. A. Zwijnenburg and A. I. Cooper, Photocatalytic hydrogen evolution from water using fluorene and dibenzothiophene sulfone-conjugated microporous and linear polymers, *Chem. Mater.*, 2018, **31**, 305–313, DOI: **10.1021/acs.chemmater.8b02833**.

63 W. Zhao, P. Yan, B. Li, M. Bahri, L. Liu, X. Zhou, R. Clowes, N. D. Browning, Y. Wu, J. W. Ward and A. I. Cooper, Accelerated Synthesis and Discovery of Covalent Organic Framework Photocatalysts for Hydrogen Peroxide Production, *J. Am. Chem. Soc.*, 2022, **144**, 9902–9909, DOI: **10.1021/jacs.2c02666**.

64 T. H. Weng, M. G. Mohamed, S. U. Sharma, I. M. A. Mekhemer, H. H. Chou and S. W. Kuo, Rationally Engineered Ultrastable Three-Dimensional (3D) Conjugated Microporous Polymers Containing Triptycene, Tetraphenylethene, and Benzothiadiazole Units as Exceptional High-Performance Organic Electrodes for Supercapacitors, *ACS Appl. Energy Mater.*, 2023, **6**, 9012–9024, DOI: **10.1021/acsaem.3c01933**.

65 M. G. Mohamed, H. Y. Hu, M. Madhu, M. Ejaz, S. U. Sharma, W. L. Tseng, M. M. Samy, C. W. Huang, J. T. Lee and S. W. Kuo, Construction of ultrastable conjugated microporous polymers containing thiophene and fluorene for metal ion sensing and energy storage, *Micromachines*, 2022, **13**, 1466, DOI: **10.3390/mi13091466**.

66 M. G. Mohamed, S. V. Chaganti, S. U. Sharma, M. M. Samy, M. Ejaz, J. T. Lee, K. Zhang and S. W. Kuo, Constructing Conjugated Microporous Polymers Containing the Pyrene-4,5,9,10-Tetraone Unit for Energy Storage, *ACS Appl. Energy Mater.*, 2022, **5**, 10130–10140, DOI: **10.1021/acsaem.2c01842**.

67 M. G. Mohamed, M. M. Samy, T. H. Mansoure, S. U. Sharma, M. S. Tsai, J. H. Chen, J. T. Lee and S. W. Kuo, Dispersions of 1,3,4-Oxadiazole-Linked Conjugated Microporous Polymers with Carbon Nanotubes as a High-Performance Electrode for Supercapacitors, *ACS Appl. Energy Mater.*, 2022, **5**, 3677–3688, DOI: **10.1021/acsaem.2c00100**.

68 W. Lyu, C. Yan, Z. Chen, J. Chen, H. Zuo, L. Teng, H. Liu, L. Wang and Y. Liao, Spirobifluorene-based conjugated microporous polymer-grafted carbon nanotubes for efficient supercapacitive energy storage, *ACS Appl. Energy Mater.*, 2022, **5**, 3706–3714, DOI: **10.1021/acsaem.2c00151**.

69 A. O. Mousa, M. G. Mohamed, Z. I. Lin, C. H. Chuang, C. K. Chen and S. W. Kuo, Conjugated microporous polymers as a novel generation of drug carriers: A systemic study toward efficient carriers of tetracycline antibiotic, *Eur. Polym. J.*, 2023, **196**, 112254, DOI: **10.1016/j.eurpolymj.2023.112254**.

70 M. Bélières, V. Sartor, P.-L. Fabre, R. Poteau, G. Bordeau and N. Chouini-Lalann, Simple electron donor molecules based on triphenylamine and carbazole derivatives, *Dyes Pigm.*, 2018, **153**, 275–283, DOI: **10.1016/j.dyepig.2018.02.022**.

71 P. Agarwala and D. Kabra, A review on triphenylamine (TPA) based organic hole transport materials (HTMs) for dye sensitized solar cells (DSSCs) and perovskite solar cells (PSCs): Evolution and molecular engineering, *J. Mater. Chem. A*, 2017, **5**, 1348–1373, DOI: **10.1039/C6TA08449D**.

72 Y. K. Wang, Z. C. Yuan, G. Z. Shi, Y. X. Li, Q. Li, F. Hui, B. Q. Sun, Z. Q. Jiang and L. S. Liao, Dopant-Free Spiro-Triphenylamine/Fluorene as Hole-Transporting Material for Perovskite Solar Cells with Enhanced Efficiency and Stability, *Adv. Funct. Mater.*, 2016, **26**, 1375–1381, DOI: **10.1002/adfm.201504245**.

73 K. Wu, X. Y. Liu, M. Xie, P. W. Cheng, J. Zheng, W. Lu and D. Li, Rational design of D–π–A–π–D porous organic polymer with polarized π for photocatalytic aerobic oxidation, *Appl. Catal., B*, 2023, **334**, 122847–122857, DOI: **10.1016/j.apcatb.2023.122847**.

74 Z. P. Li, T. Q. Deng, S. Ma, Z. W. Zhang, G. Wu, J. A. Wang, Q. Z. Li, H. Xia, S. W. Yang and X. M. Liu, Three-component donor–π–acceptor covalent–organic frameworks for boosting photocatalytic hydrogen evolution, *J. Am. Chem. Soc.*, 2023, **145**, 8364–8374, DOI: **10.1021/jacs.2c11893**.

75 C. Han, S. Xiang, S. Jin, C. Zhang and J. X. Jiang, Rational design of conjugated microporous polymer photocatalysts with definite D–π–A structures for ultrahigh photocatalytic hydrogen evolution activity under natural sunlight, *ACS Catal.*, 2023, **13**, 204–212, DOI: **10.1021/acscatal.2c04993**.

76 G. Tang, X. Huang, T. Song, S. Yin, B. Long and G. J. Deng, Alkyne bridge engineering of donor–π–acceptor polymers for efficient CO_2 reduction to CH_4 and C_2H_4 under visible light illumination, *Appl. Catal., B*, 2024, **342**, 123392, DOI: **10.1016/j.apcatb.2023.123392**.

77 L. Liu, M. A. Kochman, Y. Xu, M. A. Zwijnenburg, A. I. Cooper and R. S. Sprick, Acetylene-linked conjugated polymers for sacrificial photocatalytic hydrogen evolution from Water, *J. Mater. Chem. A*, 2021, **9**, 17242–17248, DOI: **10.1039/d1ta04288b**.

78 H. J. Sun, I. H. Oner, T. Wang, T. Zhang, O. Selyshchev, C. Neumann, Y. B. Fu, Z. Q. Liao, S. Q. Xu, Y. Hou, A. Turchanin, D. R. T. Zahn, E. Zschech, I. M. Weidinger, J. Zhang and X. L. Feng, Molecular Engineering of Conjugated Acetylenic Polymers for Efficient Cocatalyst-free Photoelectrochemical Water Reduction, *Angew. Chem., Int. Ed.*, 2019, **58**, 10368–10374, DOI: **10.1002/anie.201904978**.

79 T. Zhang, Y. Hou, V. Dzhagan, Z. Q. Liao, G. L. Chai, M. Loffler, D. Olianas, A. Milani, S. Q. Xu, M. Tommasini, D. R. T. Zahn, Z. K. Zheng, E. Zschech, R. Jordan and X. L. Feng, Conjugated Acetylenic Polymers Grafted Cuprous Oxide as an Efficient Z-Scheme Heterojunction for Photoelectrochemical Water Reduction, *Nat. Commun.*, 2018, **9**, 1140, DOI: **10.1002/adma.202002486**.

80 P. Pachfule, A. Acharjya, J. Roeser, T. Langenhahn, M. Schwarze, R. Schomäcker, A. Thomas and J. Schmidt, Diacetylene Functionalized Covalent Organic Framework (COF) for Photocatalytic Hydrogen Generation, *J. Am. Chem. Soc.*, 2018, **140**, 1423–1427, DOI: **10.1021/jacs.7b11255**.

81 X.-H. Zhang, X.-P. Wang, J. Xiao, S.-Y. Wang, D.-K. Huang, X. Ding, Y.-G. Xiang and H. Chen, Synthesis of 1,4-diethynylbenzene-based conjugated polymer photocatalysts and their enhanced visible/near-infrared-light-driven hydrogen production activity, *J. Catal.*, 2017, **350**, 64–71, DOI: **10.1016/j.jcat.2017.02.026**.

82 M. G. Mohamed, W. C. Chang and S. W Kuo, Crown Ether- and Benzoxazine-Linked Porous Organic Polymers Displaying Enhanced Metal Ion and CO_2 Capture through Solid-State Chemical Transformation, *Macromolecules*, 2022, **55**, 7879–7892, DOI: **10.1021/acs.macromol.2c01216**.

83 M. G. Mohamed, T. C. Chen and S. W. Kuo, Solid-State Chemical Transformations to Enhance Gas Capture in Benzoxazine-Linked Conjugated Microporous Polymers, *Macromolecules*, 2021, **54**, 5866–5877, DOI: **10.1021/acs.macromol.1c00736**.

84 A. O. Mousa, Z. I. Lin, S. V. Chaganti, C. H. Chuang, C. K. Chen, S. W. Kuo and M. G. Mohamed, Bifunctional imidazolium linked tetraphenylethene based conjugated microporous polymers for dynamic antibacterial properties and supercapacitor electrodes, *Polym. Chem.*, 2024, **15**, 397–411, DOI: **10.1039/D3PY01303K**.

85 M. G. Mohamed, W. C. Chang, S. V. Chaganti, S. U. Sharma, J. T. Lee and S. W. Kuo, Dispersion of ultrastable crown-ether-functionalized triphenylamine and pyrene-linked porous organic conjugated polymers with single-walled carbon nanotubes as high-performance electrodes for supercapacitors, *Polym. Chem.*, 2023, **14**, 4589–4601, DOI: **10.1039/D3PY00708A**.

86 M. G. Mohamed, S. U. Sharma, C. H. Yang, M. M. Samy, A. A. K. Mohammed, S. V. Chaganti, J. T. Lee and S. W. Kuo, Anthraquinone-Enriched Conjugated Microporous Polymers as Organic Cathode Materials for High-Performance Lithium-Ion Batteries, *ACS Appl. Energy Mater.*, 2021, **4**, 14628–14639, DOI: **10.1021/acsaem.1c03270**.

87 M. G. Mohamed, T. H. Mansoure, M. M. Samy, Y. Takashi, A. A. K. Mohammed, T. Ahamad, S. M. Alshehri, J. Kim, B. M. Matsagar, K. C. W. Wu and S. W. Kuo, Ultrastable Conjugated Microporous Polymers Containing Benzobisthiadiazole and Pyrene Building Blocks for Energy Storage Applications, *Molecules*, 2022, **27**, 2025, DOI: **10.3390/molecules27062025**.

88 M. Sachs, H. Cha, J. Kosco, C. M. Aitchison, L. Francàs, S. Corby, C. L. Chiang, A. A. Wilson, R. Godin, A. F. Williams, A. I. Cooper, R. S. Sprick, I. McCulloch and J. R. Durrant, Tracking Charge Transfer to Residual Metal Clusters in Conjugated Polymers for Photocatalytic Hydrogen Evolution, *J. Am. Chem. Soc.*, 2020, **142**, 14574–14587, DOI: **10.1021/jacs.0c06104**.

89 J. Kosco, M. Sachs, R. Godin, M. Kirkus, L. Francas, M. Bidwell, M. Qureshi, D. Anjum, J. R. Durrant and I. McCulloch, The Effect of Residual Palladium Catalyst Contamination on the Photocatalytic Hydrogen Evolution Activity of Conjugated Polymers, *Adv. Energy Mater.*, 2018, **8**, 1802181, DOI: **10.1002/aenm.201802181**.

90 M. Frisch, G. Trucks, H. Schlegel, G. Scuseria, M. Robb, J. Cheeseman, G. Scalmani, V. Barone, G. Petersson and H. Nakatsuji, *Gaussian 16*, Gaussian, Inc., Wallingford, CT, 2016.

91 R. Dennington, T. Keith and J. Millam, *GaussView, version 5*, 2009.
92 A. D. Becke, Density-functional thermochemistry. III. The role of exact exchange, *J. Chem. Phys.*, 1993, **98**, 5648–5652, DOI: **10.1063/1.464913**.
93 C. Lee, W. Yang and R. G. Parr, Development of the Colle-Salvetti correlation-energy formula into a functional of the electron density, *Phys. Rev. B*, 1988, **37**, 785–789, DOI: **10.1103/PhysRevB.37.785**.
94 R. E. Stratmann, G. E. Scuseria and M. J. Frisch, An efficient implementation of time-dependent density-functional theory for the calculation of excitation energies of large molecules, *J. Chem. Phys.*, 1998, **109**, 8218–8224, DOI: **10.1063/1.477483**.
95 N. M. O'boyle, A. L. Tenderholt and K. M. Langner, Cclib: a library for package-independent computational chemistry algorithms, *J. Comput. Chem.*, 2008, **29**, 839–845, DOI: **10.1002/jcc.20823**.
96 H. Chermette, Chemical reactivity indexes in density functional theory, *J. Comput. Chem.*, 1999, **20**, 129–154, DOI: **10.1002/(SICI)1096-987X(19990115)20:1<129::AID-JCC13>3.0.CO;2-A**.
97 R. Zaier and S. Ayachi, DFT molecular modeling studies of D-π-A-π-D type cyclopentadithiophene-diketopyrrolopyrrole based small molecules donor materials for organic photovoltaic cells, *Optik*, 2021, **239**, 166787, DOI: **10.1016/j.ijleo.2021.166787**.
98 A. Tiwari and U. Pal, Effect of donor–donor–π–acceptor architecture of triphenylamine-based organic sensitizers over TiO_2 photocatalysts for visible-light-driven hydrogen production, *Int. J. Hydrog. Energy*, 2015, **40**, 9069–9079, DOI: **10.1016/j.ijhydene.2015.05.101**.
99 X. Lan, X. Liu, Y. Zhang, Q. Li, J. Wang, Q. Zhang and G. Bai, Unveiling Charge Dynamics in Alkynyl-Bridged Donor–π–Acceptor Covalent Triazine Framework for Enhanced Photoredox Catalysis, *ACS Catal.*, 2021, **11**, 7429–7441, DOI: **10.1021/acscatal.1c01794**.
100 T. Mestiri and K. Alimi, DFT and TD-DFT design of small π-conjugated molecules with narrow band gap and high efficiency for organic solar cells, *Theor. Chem. Acc.*, 2018, **137**, 1–10, DOI: **10.1007/s00214-018-2321-1**.
101 H. Etabti, A. Fitri, A. T. Benjelloun, M. Benzakour and M. Mcharfi, Efficient tuning of benzocarbazole based small donor molecules with D-π-A-π-D configuration for high-efficiency solar cells *via* π-bridge manipulation: A DFT/TD-DFT study, *Comput. Theor. Chem.*, 2022, **1208**, 113580, DOI: **10.1016/j.comptc.2021.113580**.
102 S. B. Yadav, S. S. Sonvane and N. Sekar, Novel blue-green emitting NLOphoric triphenylamine-imidazole based donor–π–acceptor compound: Solvatochromism, DFT, TD-DFT and non-linear optical studies, *Spectrochim. Acta, Part A*, 2020, **224**, 117421, DOI: **10.1016/j.saa.2019.117421**.
103 C. Adamo and D. Jacquemin, The calculations of excited-state properties with Time-Dependent Density Functional Theory, *Chem. Soc. Rev.*, 2013, **42**, 845–856, DOI: **10.1039/C2CS35394F**.

